GOLD
OPEN ACCESS

THE GEOLOGICAL SOCIETY OF AMERICA®

Revised age and regional correlations of Cenozoic strata on Bat Mountain, Death Valley region, California, USA, from zircon U-Pb geochronology of sandstones and ash-fall tuffs

Theresa M. Schwartz[1], A. Kate Souders[2], Jens-Erik Lundstern[1], Amy K. Gilmer[1], and Ren A. Thompson[1]

[1]U.S. Geological Survey, Geosciences and Environmental Change Science Center, Denver, 80225 Colorado, USA
[2]U.S. Geological Survey, Geology, Geophysics, and Geochemistry Science Center, Denver, 80225 Colorado, USA

ABSTRACT

Basin analysis and tectonic reconstructions of the Cenozoic history of the Death Valley region, California, USA, are hindered by a lack of volcanic (tuff) age control in many stratigraphic successions exposed in the Grapevine and Funeral Mountains of California, USA. Although maximum depositional ages (MDAs) interpreted from detrital zircon U-Pb data may be a promising alternative to volcanic ages, arguments remain regarding the calculation of MDAs including, but not limited to, the number of "young" grains to consider (i.e., the spectrum of dates used to calculate the MDA); which grains, if any, should be ignored; which approaches yield results that are statistically rigorous; and ultimately, which approaches result in ages that are geologically reasonable. We compare commonly used metrics of detrital zircon MDA for five sandstone samples from the Cenozoic strata exposed on Bat Mountain in the southern Funeral Mountains of California—i.e., the youngest single grain (YSG), the weighted mean of the youngest grain cluster of two or more grains at 1σ uncertainty (YC1σ(2+)) and of three or more grains at 2σ uncertainty (YC2σ(3+)), the youngest graphical peak (YPP), and the maximum likelihood age (MLA). Every sandstone sample yielded abundant Cenozoic zircon U-Pb dates that formed unimodal, near-normal age distributions that were clearly distinguishable from the next-oldest grains in each sample and showed an apparent up-section decrease in peak age. Benchmarked against published K/Ar and ⁴⁰Ar/³⁹Ar ages and five new zircon U-Pb ages of ash-fall tuffs, our analysis parallels prior studies and demonstrates that many MDA metrics—YSG, YC1σ(2+), YC2σ(3+), and YPP—drift toward unreasonably young or old values. In contrast, the maximum likelihood estimation approach and the resulting MLA metric consistently produce geologically appropriate estimates of MDA without arbitrary omission of any young (or old) zircon dates. Using the MLAs of sandstones and zircon U-Pb ages of interbedded ash-fall tuffs, we develop a new age model for the Oligocene–Miocene Amargosa Valley Formation (deposited ca. 28.5–18.5 Ma) and the Miocene Bat Mountain Formation (deposited ca. 15.5–13.5 Ma) and revise correlations to Cenozoic strata across the eastern Death Valley region.

■ INTRODUCTION

Discontinuously exposed and heavily deformed outcrops of Cenozoic strata in the Death Valley region of California, USA, chronicle a complex history of extension, uplift, basin formation, and volcanism. Existing tectonostratigraphic models for the region broadly focus on two phases of Cenozoic basin evolution, including an Eocene to early Miocene phase that largely predated Basin and Range-style extension (e.g., Çemen et al., 1999; Fridrich and Thompson, 2011; Miller et al., 2022) with some lower-magnitude extension locally (e.g., Snow and Lux, 1999; Sizemore et al., 2019; Midttun, 2022) and a middle Miocene-to-Pliocene phase that was synchronous with the progression of Basin and Range extension through the Death Valley region (e.g., Çemen et al., 1999; Snow and Lux, 1999; Wright et al., 1999; Niemi et al., 2001; Miller and Pavlis, 2005; Fridrich and Thompson, 2011). Refining the timing, causes, and paleogeography associated with these events involves detailed comparisons of stratigraphic successions that have been heavily dissected, offset, and deformed by post- and/or syn-depositional extension, which fundamentally requires individual sections to have good age control.

The Death Valley region is host to voluminous and widespread volcanic rocks, but local volcanism associated with the southwest Nevada and central Death Valley volcanic fields did not initiate until the middle Miocene (Wright et al., 1991; Sawyer et al., 1994; Fridrich and Thompson, 2011). While middle Miocene and younger strata in the Death Valley region are commonly associated with primary volcanic rocks that provide age control for coeval sediments (e.g., Çemen et al., 1985; Fridrich et al., 2012), pre-middle Miocene strata are inherently more difficult to date because they lack interbedded tuffs. Some pre-middle Miocene strata contain sparse ash-fall tuffs that are interpreted to have emanated from distant caldera complexes of the Great Basin, but the tuffs are not spatially or temporally ubiquitous and become less prevalent in older stratigraphic intervals. As an alternative, recent studies have explored the

Theresa Schwartz (iD) https://orcid.org/0000-0001-6606-4072

utility of detrital zircon U-Pb geochronology in constraining the depositional age of Eocene strata in the Death Valley region (Midttun, 2022; Miller et al., 2022). Those studies interpreted Cenozoic detrital zircon grains to be nearly syn-depositional in age, thereby providing age constraints for stratigraphic intervals that otherwise lack volcanic deposits. Their results suggest that maximum depositional ages (MDAs) interpreted from detrital zircon data may be critical for resolving the age of pre-middle Miocene strata in the Death Valley region. However, they also prompt questions regarding (1) the interpretive methods used in determining MDAs, and (2) the accuracy and utility of those ages compared to those of ash-fall tuffs.

We address these questions using zircon U-Pb geochronology data for a suite of 10 sandstone and ash-fall tuff samples from Oligocene(?) to Miocene strata exposed on Bat Mountain in the southern Funeral Mountains of California (Figs. 1 and 2). We interpret the new geochronology data in the context of a detailed, composite measured section to provide stratigraphic control for all samples. Commonly used detrital zircon MDA metrics are compared for individual sandstone samples to determine which are most statistically and geologically reasonable, and interpreted MDAs are compared against the zircon U-Pb ages of ash-fall tuff samples to assess stratigraphic consistency. Collectively, the interpreted ash ages and detrital zircon MDAs provide a detailed age model for the Amargosa Valley and Bat Mountain formations and their constituent informal lithologic members, permitting enhanced stratigraphic correlation to Cenozoic strata exposed throughout the Death Valley region and elsewhere in the Great Basin.

■ STUDY AREA

Eocene to Pliocene strata are intermittently exposed in the northwest–southeast-trending structural blocks of the Grapevine and Funeral Mountains on the eastern margin of Death Valley National Park (Fig. 1). Bat Mountain forms the southeasternmost structural block in the southern Funeral Mountains and hosts a >1000-m-thick succession of Oligocene(?) to Miocene strata (Figs. 2 and 3). The range is bound on the north, east, and south by a series of normal faults and dextral strike-slip faults (Fig. 2; Fridrich et al., 2012) that together accommodated the development of late Neogene-to-present transtensional basins of the southwestern Basin and Range Province (Snow and Lux, 1999; Fridrich and Thompson, 2011). Bat Mountain is structurally separated from westward-adjacent parts of the southern Funeral Mountains by a series of north–northeast-striking normal faults that down-drop adjacent structural blocks to the west (Fig. 2). We focus on Cenozoic strata exposed at the northern end of Bat Mountain because all units are well-exposed in their original stratigraphic order (Fig. 3).

Cenozoic strata of Bat Mountain include the Oligocene(?) to lower Miocene Amargosa Valley Formation, the lower(?) to middle(?) Miocene Kelley's Well Limestone, and the middle Miocene Bat Mountain Formation (Figs. 2 and 3; Çemen et al., 1985, 1999). These strata unconformably overlie Paleozoic
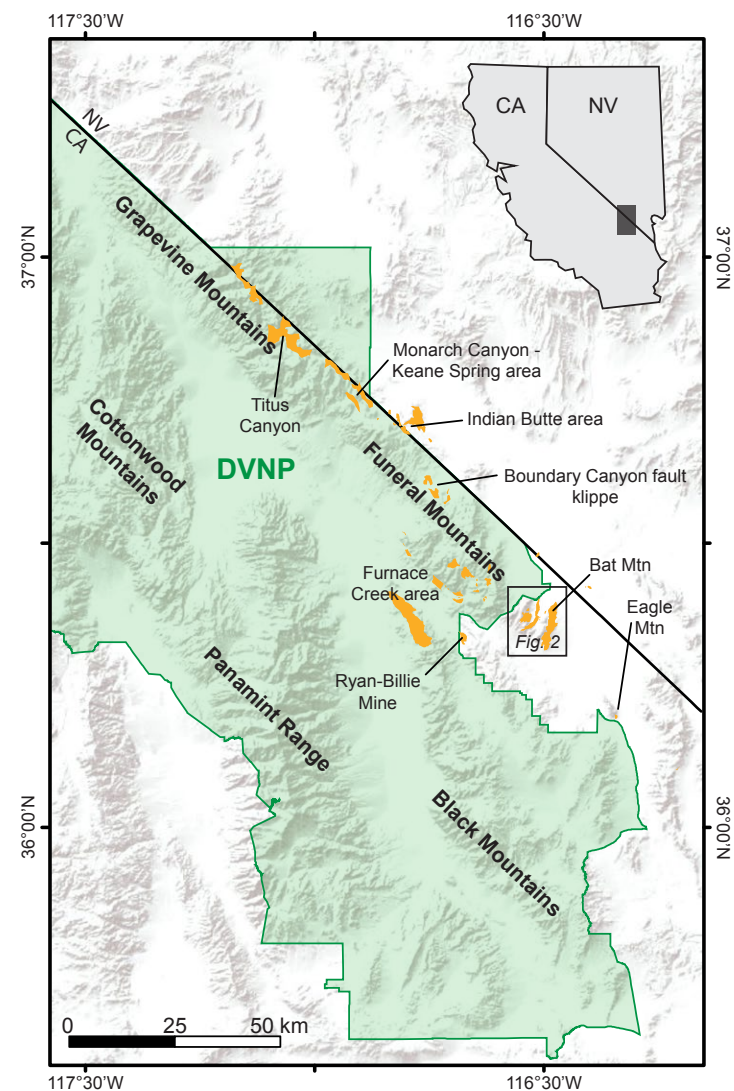

Figure 1. Context map showing the physiography of the area within and surrounding Death Valley National Park (DVNP), California and Nevada, USA. Localities of Cenozoic strata of the Grapevine and Funeral Mountains that are specifically mentioned in this study are represented by orange polygons and labeled with black callouts (from Wright and Troxel, 1993; Workman et al., 2002; Fridrich et al., 2012).
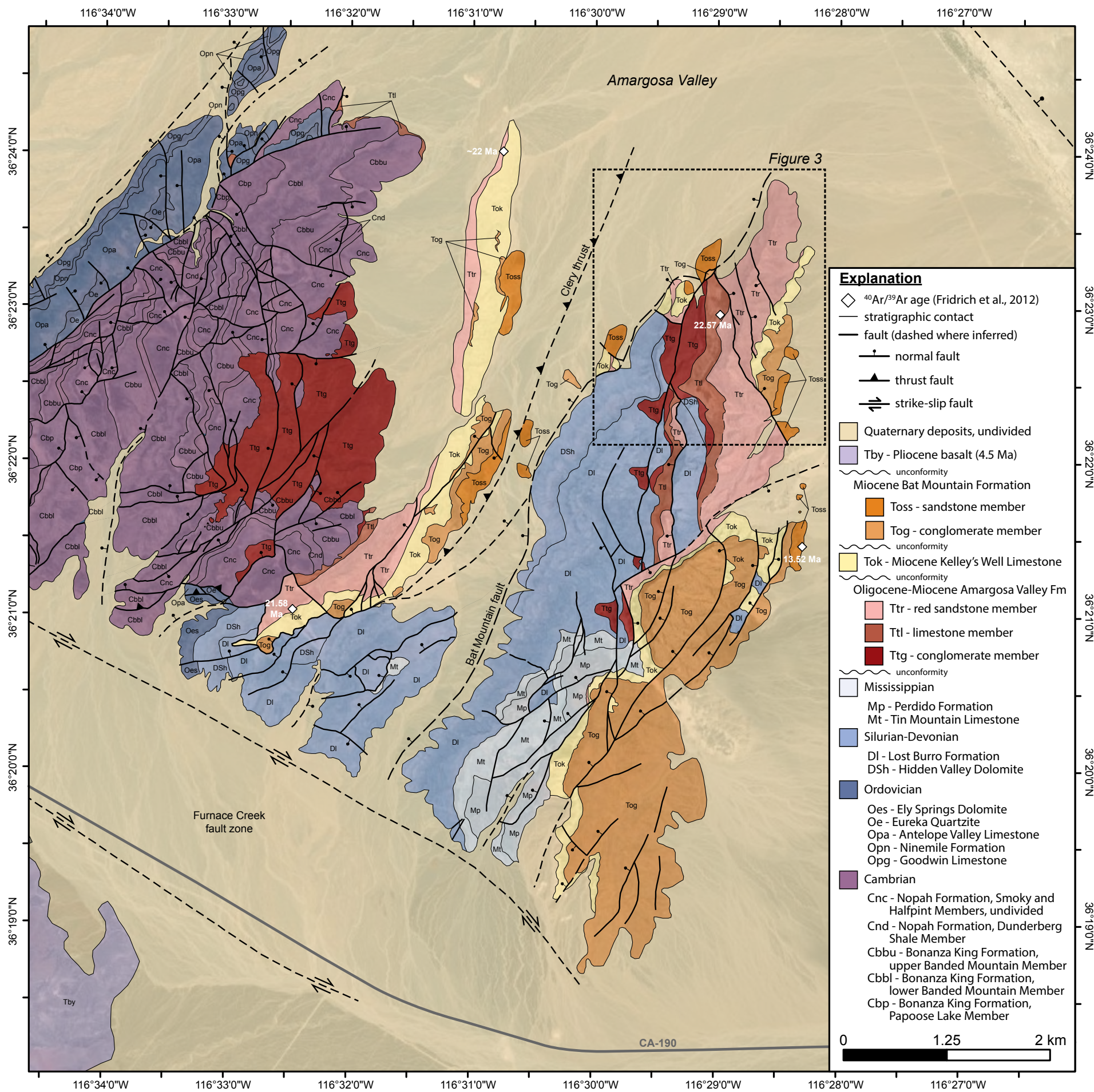
Figure 2. Geologic map of Bat Mountain and adjacent structural culminations in the southern Funeral Mountains (modified from Fridrich et al., 2012).
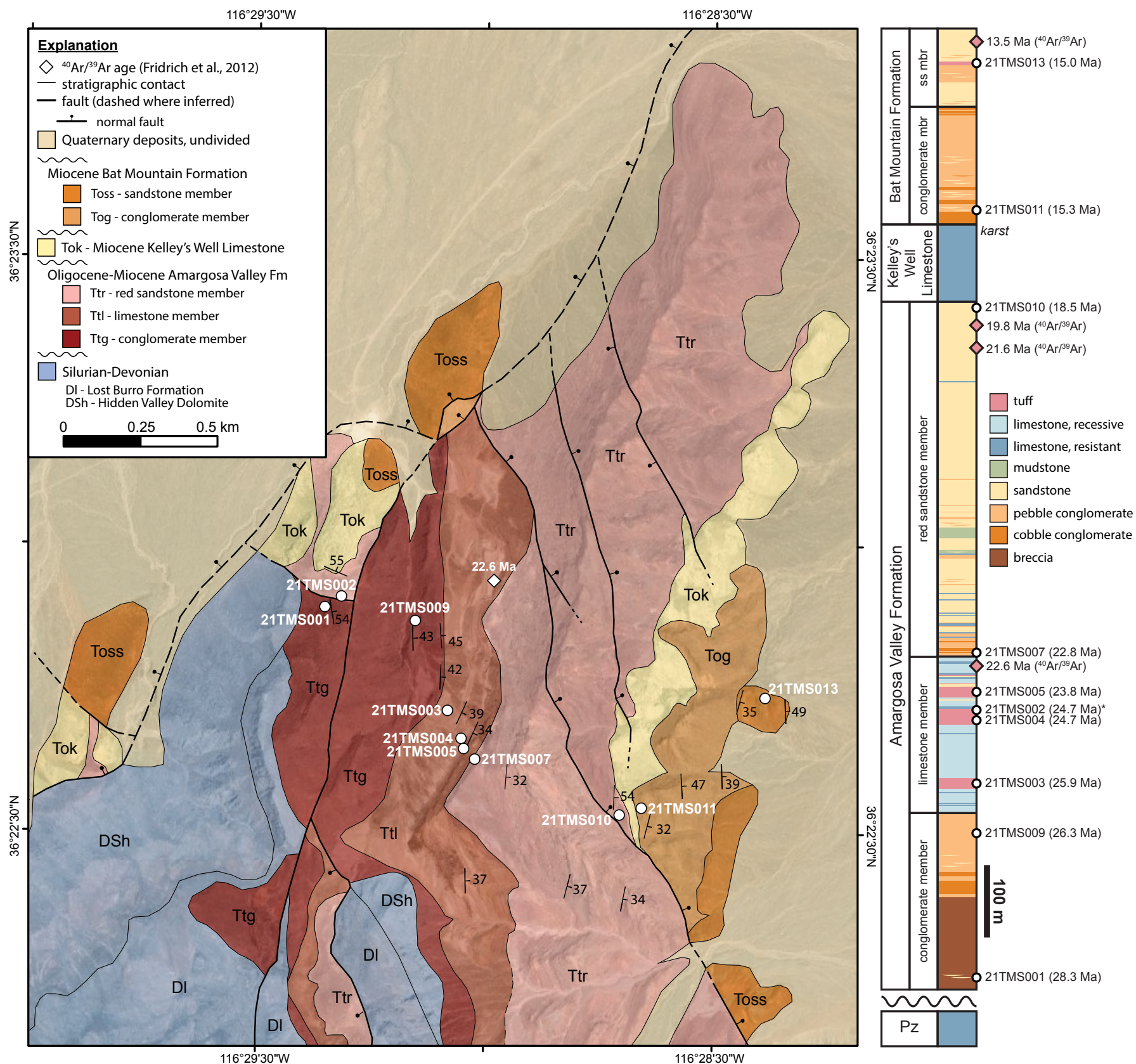
Figure 3. Detailed geologic map of the northern end of Bat Mountain (modified from Fridrich et al., 2012) showing refined contacts between the Cenozoic Amargosa Valley Formation, Kelley's Well Limestone, Bat Mountain Formation, and their constituent lithologic members. A composite stratigraphic section through all Cenozoic units, corrected for fault offset and duplication, is shown at right. The section was measured from west to east across the outcrop belt, with the general transect noted on the map by tuff and sandstone sample locations (white circles) and strike-and-dip symbols. Sample locations are provided in Table 1. Ash-fall tuff sample 21TMS002, notated with an asterisk, was collected from an exposure previously mapped as the red sandstone member of the Amargosa Valley Formation (Fridrich et al., 2012) but is interpreted herein as part of the limestone member of the Amargosa Valley Formation based on the zircon U-Pb age presented. Pz—Paleozoic; ss—sandstone.

miogeoclinal rocks that form the lower plate of the Mesozoic Clery thrust (Figs. 2 and 3; Fridrich et al., 2012). Paleozoic and Cenozoic strata are strongly dissected, uplifted, and tilted along a series of closely spaced, north–northeast- to north–northwest-striking normal faults associated with late Miocene and later transtension (Figs. 2 and 3; Fridrich et al., 2012).

We adopt the map-unit nomenclature of Çemen et al. (1999) and subdivide the exposures of the Amargosa Valley Formation into three informal members including, from oldest to youngest, a conglomerate member, a limestone member, and a red sandstone member (Figs. 2 and 3). The conglomerate member is ~225 m thick (Fig. 3) and records deposition in a coarse-grained alluvial fan-dominated environment with clast derivation from locally exposed Paleozoic strata (Fig. 4C; Çemen et al., 1985). Alluvial fan deposits are abruptly overlain by the ~200-m-thick limestone member (Figs. 3 and 4A), which represents a lacustrine environment characterized primarily by carbonate deposition (Çemen et al., 1985). K/Ar (biotite) and ^{40}Ar/^{39}Ar (sanidine) ages of tuff layers near the base and top of the limestone member, respectively, constrain its age to between 24.7 ± 0.3 Ma (2σ; Çemen et al., 1985) and 22.57 ± 0.1 Ma (2σ; Fridrich et al., 2012). The limestone member is overlain by the red sandstone member, which is marked by the abrupt appearance of thickly amalgamated fluvial sandstone and conglomerate reaching 450 m thick (Figs. 3 and 4A; Çemen et al., 1985). Notably, thin limestone beds are present throughout the lower 100 m of the red sandstone member (Fig. 3), which indicates that the transition from lacustrine environments to fluvial environments was gradual. Deposition of the red sandstone member continued until ca. 21.58 ± 0.16 Ma (2σ), based on an ^{40}Ar/^{39}Ar (sanidine) age of a tuff near the top of the member (Fridrich et al., 2012), and as late as ca. 19.80 ± 0.20 Ma (2σ) based on a K/Ar (biotite) age of a tuff (Çemen et al., 1985) from an unspecified location.

The Amargosa Valley Formation is overlain by the Kelley's Well Limestone along the entire length of the Bat Mountain block, but the contact varies in character. The Kelley's Well Limestone lies with subtle angular unconformity on the Amargosa Valley Formation on the southern side of Bat Mountain, reflecting tilting and erosion of the Amargosa Valley Formation prior to deposition of the Kelley's Well Limestone (Çemen et al., 1999; Fridrich and Thompson, 2011). Across the exposures depicted in Figure 3, the red sandstone member of the Amargosa Valley Formation and the Kelley's Well Limestone generally appear conformable based on concordant bedding in the two formations (Çemen et al., 1985).

The Kelley's Well Limestone is disconformably overlain by the Bat Mountain Formation. Although bedding appears concordant across the formation boundary (e.g., Fig. 3), a paleo-karst horizon at the top of the Kelley's Well Limestone (Fig. 4D) reveals a depositional hiatus and erosion prior to deposition of the Bat Mountain Formation. Unconformity between the two formations is also suggested by the presence of clasts of Kelley's Well Limestone in conglomerate of the Bat Mountain Formation (Çemen et al., 1985). The Bat Mountain Formation is subdivided into two informal members, a lower conglomerate member and an upper sandstone member, that together form a 250-m-thick succession of interfingering alluvial fan and fluvial deposits (Fig. 3; Çemen

et al., 1985; Fridrich et al., 2012). An ^{40}Ar/^{39}Ar (sanidine) age of a tuff from the uppermost exposures of the sandstone member suggests deposition of the Bat Mountain Formation until at least 13.52 ± 0.07 Ma (2σ; Fridrich et al., 2012). The top of the Bat Mountain Formation is buried beneath Quaternary alluvium of the Amargosa Valley (Fig. 2).

■ METHODS

Field Methods and Sample Collection

Using existing 1:50,000 scale geologic mapping of the southern Funeral Mountains by Fridrich et al. (2012) and high-resolution satellite imagery, we refined the lithostratigraphic contacts of lower Cenozoic deposits preserved in the Bat Mountain structural block (Figs. 2 and 3). Figure 3 displays a composite stratigraphic section through the Amargosa Valley Formation, Kelley's Well Limestone, and Bat Mountain Formation, which we measured at 1–5 m resolution to document vertical trends in lithology and to provide a stratigraphic framework for sampling of sandstones and interstratified tuffs. Based on the lithostratigraphy, we correlated individual measured sections in the field to account for stratigraphic complexities related to faults and topographic barriers. Within that stratigraphic context, we collected 10 samples of tuff and sandstone to better constrain the depositional ages of the Amargosa Valley and Bat Mountain formations (Table 1, Fig. 3).

Zircon U-Pb Geochronology

Zircon U-Pb Geochronology of Tuffs

We collected five ash-fall tuff samples from the Amargosa Valley (N = 4) and Bat Mountain formations (N = 1) for zircon U-Pb analysis (Table 1). ZirChron LLC (Tucson, Arizona, USA) completed mineral separations using the following process to obtain zircon separates: electrical pulse disaggregation (EPD) of whole-rock samples to minimize the fracture of individual grains and preserve original grain morphology, density separation on a water table, density separation in methylene iodide (MEI) to remove particles with specific gravity <3.33, and magnetic separation using a Frantz magnetic separator.

We completed U-Pb analyses of zircon grains at the Texas Tech University Mineral Isotope Laser Laboratory using a Nu Plasma AttoM magnetic sector inductively coupled plasma–mass spectrometer (ICP-MS) coupled to an ESI NWR 193UC laser ablation (LA) system consisting of a TwoVol2 ablation chamber and a Coherent Excistar 193 nm ArF excimer laser. Zircons were hand-picked from the non-magnetic fraction of heavy mineral separate, mounted in a 25 mm epoxy grain mount, and polished to the center. A 15 µm laser spot was used for all analyses and placed on regions of zircon grains free of fractures, inclusions, or overgrowths, guided by cathodoluminescence (CL) images.
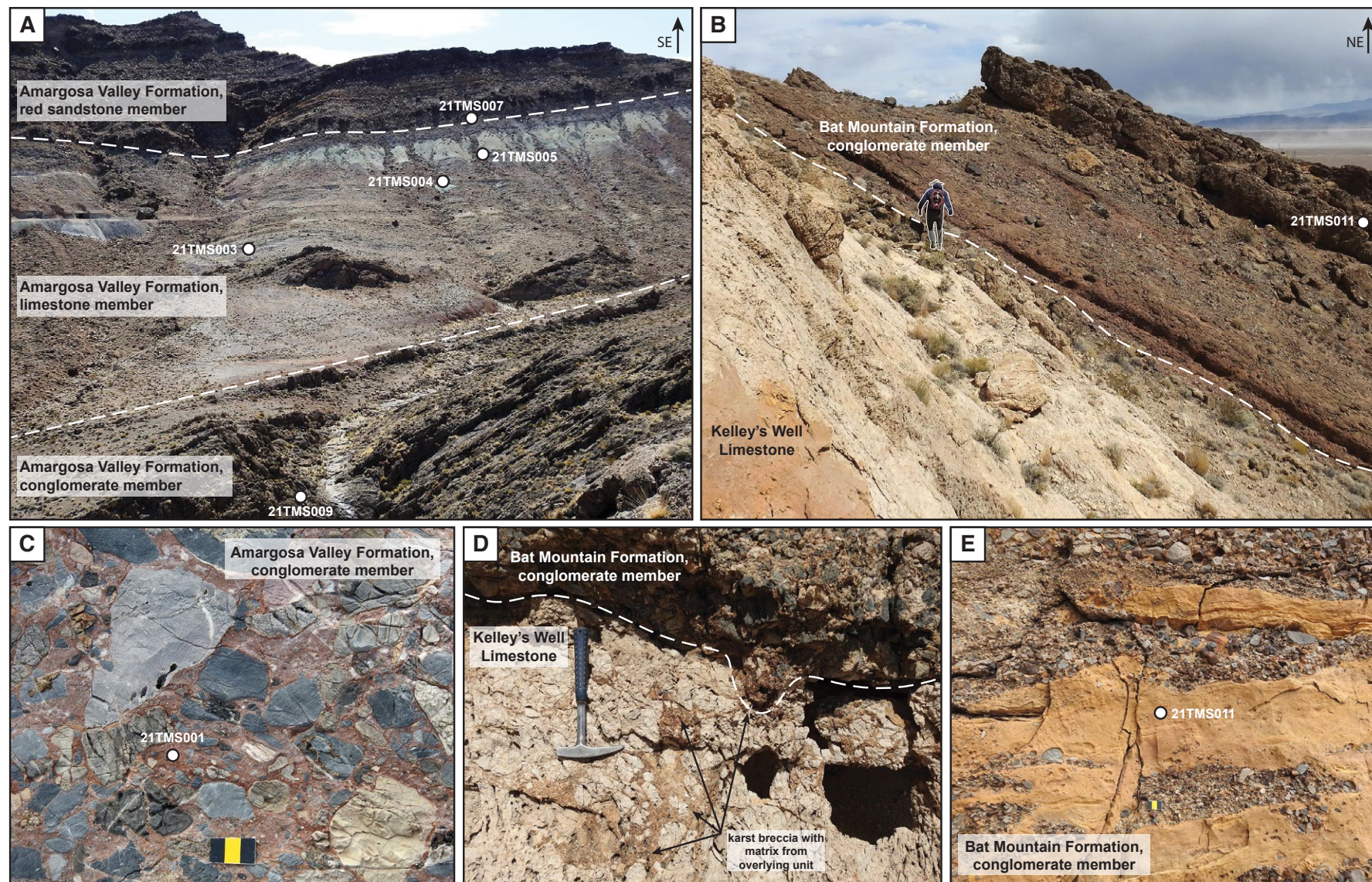
Figure 4. Outcrop photographs of the Amargosa Valley and Bat Mountain formations, with tuff and detrital zircon sample locations highlighted by white circles. (A) Stratigraphic succession including the conglomerate, limestone, and red sandstone members of the Amargosa Valley Formation. (B) Stratigraphic succession showing the conglomerate member of the Bat Mountain Formation where it disconformably overlies the Kelley's Well Limestone. (C) Photograph of a limestone breccia with sandstone matrix at the base of the Amargosa Valley Formation; scale is 3 cm wide. (D) Photograph of the karst horizon at the contact between the Kelley's Well Limestone and Bat Mountain Formation. (E) Photograph of a conglomerate with sandstone lenses near the base of the Bat Mountain Formation; scale is 3 cm wide.

TABLE 1. LOCATION INFORMATION FOR NEW TUFF AND SANDSTONE SAMPLES PRESENTED IN THIS STUDY

Sample name	Formation	Member	Lithology	Latitude (°N, WGS 1984)	Longitude (°W, WGS 1984)	Preferred MDA (Ma, 2σ)
21TMS001	Amargosa Valley Formation	Conglomerate member (base)	Sandstone	36.3815	116.4892	28.34 ± 0.24
21TMS009	Amargosa Valley Formation	Conglomerate member (top)	Sandstone	36.3811	116.4859	26.26 ± 0.22
21TMS003	Amargosa Valley Formation	Limestone member (lower)	Ash-fall tuff	36.3785	116.4847	25.87 ± 0.04
21TMS004	Amargosa Valley Formation	Limestone member (middle)	Ash-fall tuff	36.3777	116.4842	24.65 ± 0.07
21TMS002	Amargosa Valley Formation	Limestone member (unknown position)	Ash-fall tuff	36.3818	116.4886	24.65 ± 0.06
21TMS005	Amargosa Valley Formation	Limestone member (upper)	Ash-fall tuff	36.3774	116.4841	23.79 ± 0.06
21TMS007	Amargosa Valley Formation	Red sandstone member (base)	Sandstone	36.3771	116.4837	22.79 ± 0.19
21TMS010	Amargosa Valley Formation	Red sandstone member (top)	Sandstone	36.3755	116.4784	18.49 ± 0.36
21TMS011	Bat Mountain Formation	Conglomerate member (base)	Sandstone	36.3757	116.4776	15.30 ± 0.15
21TMS013	Bat Mountain Formation	Sandstone member (lower)	Ash-fall tuff	36.3789	116.4731	15.00 ± 0.05

Note: MDA—maximum depositional age; WGS—World Geodetic System.

Analytical details and instrument parameters are included in Table S1[1]. Zircon 91500 (1066.0 ± 0.6 Ma [2σ]; Wiedenbeck et al., 2004, recalculated by Horstwood et al., 2016) was used to correct for mass spectrometer bias on Pb/Pb and U-Pb isotopic ratios and downhole U/Pb fractionation (Košler et al., 2002) and to calculate U and Th concentrations from background-corrected count rates. Pb/Pb and U/Pb isotopic ages and U and Th concentrations were determined using iolite (v4) software. No common Pb correction was made to the final data. Only single analyses between 90% and 105% concordant based on comparison of the $^{206}Pb/^{238}U$ and $^{207}Pb/^{235}U$ ages with at least 5 s of data averaged over a single laser ablation analysis were used for final age calculations. U-Pb dates for the tuff samples are reported at 2σ (including both analytical and systematic uncertainty) in Table S1 and Schwartz and Souders (2022).

We analyzed five zircon secondary reference materials (SRMs; characterized by isotope dilution–thermal ionization mass spectrometry [ID-TIMS] ages) with the zircons separated from Bat Mountain tuff samples as a check and monitor on data quality: Fish Canyon Tuff zircon (28.478 ± 0.024 Ma [2σ]; Schmitz and Bowring, 2001); Plešovice zircon (337.16 ± 0.11 Ma [2σ]; Sláma et al., 2008, recalculated by Horstwood et al., 2016); R33 zircon (419.3 ± 0.4 Ma [2σ]; Black et al., 2004); 9980 zircon (1150 ± 2 Ma [2σ]; Košler et al., 2013); and Tan Brown zircon (2512.24 ± 0.71 Ma [2σ]; Bauer et al., 2020). Analytical data and concordia ages for the SRMs are listed in Table S1 (see footnote 1) and Schwartz and Souders (2022).

Detrital Zircon U-Pb Geochronology of Sandstones

We collected five sandstone samples from the Amargosa Valley (N = 4) and Bat Mountain (N = 1) formations for detrital zircon U-Pb analysis (Table 1).

We preferentially sampled medium-grained sandstone to reduce the potential effects of grain-size bias on detrital zircon age distributions, although we note that the conglomerate members of both the Amargosa Valley and Bat Mountain formations contain only poorly sorted sandstone with grain sizes ranging from very fine to very coarse. GeoSep Services (Moscow, Idaho, USA) completed mineral separations using the following process to obtain zircon separates: crushing, sieving, washing in water to remove clay particles, density separation in lithium metatungstate (LMT) to remove particles with specific gravity less than 2.95, magnetic separation using a hand magnet followed by a Frantz magnetic separator, and density separation in MEI to remove particles with specific gravity <3.33.

We measured the U-Th-Pb isotopic ratios of detrital zircon grains using laser ablation–inductively coupled plasma––mass spectrometry (LA-ICP-MS) with an Element 2 mass spectrometer at the University of Arizona LaserChron Center, Tucson, Arizona, USA, following standard analytical methods (Gehrels et al., 2008; Gehrels and Pecha, 2014). Individual zircons were ablated using a Photon Machines Analyte G2 excimer laser that delivered a 30 μm beam to hand-selected crystal locations. To prevent biasing analysis, we selected individual zircon spots from mount images using a grid pattern to capture a representative variety of grain sizes and morphologies. FC-1 zircon (ID-TIMS age of 1099.0 ± 0.6 Ma [2σ]; Paces and Miller, 1993) was used as a primary standard, with Sri Lanka (SL-M, ID-TIMS age of 563.5 ± 3.2 Ma [2σ]; Gehrels et al., 2008) and R33 (ID-TIMS age of 419.26 ± 0.39 Ma [2σ]; Black et al., 2004) zircons used as secondary standards. We targeted a total of 315 zircon grains of unknown age per sample. We excluded analyses from age interpretation if they had: $^{206}Pb/^{238}U$ ratios with >10% precision; $^{206}Pb/^{207}Pb$ ratios with >10% precision unless associated with $^{206}Pb/^{238}U$ ages of <400 Ma; 20% discordance and/or 5% reverse discordance based on apparent $^{206}Pb/^{238}U$ versus $^{206}Pb/^{207}Pb$

---

[1]Supplemental Material. Table S1: New zircon U-Pb data for tuffs of the Amargosa Valley and Bat Mountain formations exposed on Bat Mountain in the southern Funeral Mountains, California. Table S2: New detrital zircon U-Pb data for sandstones of the Amargosa Valley and Bat Mountain formations exposed on Bat Mountain in the southern Funeral Mountains, California. Please visit https://doi.org/10.1130/GEOS.S.21568818 to access the supplemental material, and contact editing@geosociety.org with any questions.

ages; and >600 Pb counts per second. Due to precision cutoffs in isotopic chronometers, we used an apparent $^{206}Pb/^{238}U$ age of 900 Ma as a threshold for "best age," in which we adopted $^{206}Pb/^{238}U$ ages for analyses <900 Ma and $^{207}Pb/^{206}Pb$ ages for analyses >900 Ma. All detrital zircon dates are reported at 1σ (including only analytical uncertainty, but with external uncertainty noted) in Table S2 (see footnote 1) and Schwartz and Souders (2022).

Maximum Depositional Age (MDA) Determination from Zircon U-Pb Data

We utilized Cenozoic U-Pb dates to calculate MDAs of all new tuff and sandstone samples. We treated the age distributions of all samples, both sedimentary and igneous, as detrital to account for the presence of non-uniform age distributions, including the presence of xenocrysts in some tuffs. We considered the interpreted MDA of each tuff sample to be its eruption age, assuming negligible time between eruption and deposition. Likewise, we considered the MDA of each sandstone sample to approximate its true depositional age, again assuming minimal time between zircon crystallization, exposure, sediment transport, and deposition (Schwartz et al., 2021).

Table 2 compares commonly used metrics of zircon MDA for all new samples presented herein. These metrics include the youngest graphical peak (YPP), the youngest single grain (YSG), and the weighted means of the youngest grain cluster of two or more grains at 1σ uncertainty (YC1σ(2+)) and of three or more grains at 2σ uncertainty (YC2σ(3+)) from Dickinson and Gehrels (2009), as well as the maximum likelihood age (MLA) of Vermeesch (2021). In addition, we introduce one variation on the MLA metric that focuses exclusively on the youngest peak in each age distribution: the central age of the youngest peak (CAYP). This variant is calculated using the same method as the central age of an entire age distribution (calculated alongside the MLA; Vermeesch, 2018, 2021), but it considers only the grains comprising the youngest peak in the age distribution (i.e., older grains were not used as inputs; Fig. 5). For tuff samples, we also present weighted mean ages (WMAs) in the text, calculated from all Cenozoic grains but allowing for outlier omission, to provide an age metric consistent with those commonly reported for igneous rocks. We note that the WMA and MLA for any given tuff sample are statistically indistinguishable at 2σ.

We calculated the MDA metrics using individual dates reported at 1σ error. We calculated metrics YPP, YC1σ(2+), and YC2σ(3+) using detritalPy (for which outputs are reported at 1σ uncertainty; Sharman et al., 2018), and metrics MLA, CAYP, and WMA using IsoplotR (for which outputs are reported at 2σ uncertainty; Vermeesch, 2018). For the MLA and CAYP calculations in IsoplotR, we accepted a logarithmic transformation and set "finite mixtures" to "minimum" in accordance with Vermeesch (2021). For sandstones whose raw detrital zircon dates are reported at 1σ and only include analytical uncertainty (Table S2, see footnote 1; Schwartz and Souders, 2022), we accounted for external sources of uncertainty by propagating error in quadrature (Horstwood et al., 2016) for each calculated MDA. The same error propagation was not performed for tuff

samples because their constituent dates are already reported at 2σ, including both analytical and external uncertainty (Table S1, see footnote 1; Schwartz and Souders, 2022). Ultimately, all MDAs for both sandstones and tuffs are reported at 2σ total uncertainty in Tables 1 and 2.

Table 2 also lists the same suite of MDA metrics for previously published zircon U-Pb data that characterize Cenozoic strata across the eastern Death Valley region (Niemi, 2013; Miller et al., 2022; Midttun, 2022). We recalculated MDAs for published data using the methods outlined above, including propagation of external uncertainties when possible, to ensure internal consistency in MDA calculations.

■ RESULTS AND INTERPRETATIONS

Tuff Geochronology

21TMS003: Lower Part of the Limestone Member, Amargosa Valley Formation

Sample 21TMS003 was collected from the lower part of a very poorly exposed, pale green ash fall tuff ~35 m above the base of the limestone member of the Amargosa Valley Formation (Figs. 3 and 4A). The 12.75-m-thick tuff is largely microcrystalline silica but also contains thin intervals of silt-sized particles near its base, including very small, copper-colored, oxidized biotite crystals. In thin-section, the tuff appears to be structureless, with sparse quartz and biotite phenocrysts in a devitrified siliceous matrix. The tuff directly overlies a gray, structureless limestone bed, consistent with deposition in a low-energy lacustrine setting. Concordant dates were acquired for 34 zircon grains, ranging from ca. 27 Ma to 25 Ma (Table S1, see footnote 1). The dates yield a WMA of 25.88 ± 0.04 Ma (2σ; n = 33/34) and a MLA of 25.87 ± 0.04 Ma (2σ; n = 34/34) (Table 2; Fig. 6A).

21TMS004: Middle Part of the Limestone Member, Amargosa Valley Formation

Sample 21TMS004 was collected from the middle of a bright white to pale green, 15-m-thick tuff in the middle part of the limestone member of the Amargosa Valley Formation (Figs. 3 and 4A), ~70 m up-section from sample 21TMS003. The tuff is generally fine-grained, crystal- and lithic grain-rich, and heavily fractured throughout. Larger phenocrysts (up to 2 mm) and volcanic lithic grains (up to 4 mm in diameter) are concentrated in the lower 1 m of the tuff. Phenocrysts include plagioclase, biotite, and euhedral to anhedral quartz in a devitrified siliceous matrix. The tuff overlies a poorly exposed interval of reddish, silty limestone and is in turn overlain by 4.5 m of indurated, fossiliferous limestone, which suggests deposition in a low-energy lacustrine setting. The upper 0.5 m of the tuff displays crude planar to undulatory lamination,

TABLE 2. COMPILATION OF K/Ar, ⁴⁰Ar/³⁹Ar, AND U-Pb AGE CONSTRAINTS FOR CENOZOIC ROCKS OF THE GRAPEVINE-FUNERAL MOUNTAINS, INCLUDING A COMPARISON OF COMMON DETRITAL ZIRCON MDA METRICS

Section (see Figs. 1, 10)	Formation	Member	Sample name	Rock type	Method	Mineral	Detrital zircon MDA metrics												Argon age (Ma)	2σ** (Ma)	Preferred age (Ma)	2σ (Ma)	Data source
							YPP (Ma)	YSG (Ma)	2σ (Ma)	YC1σ(2+) (Ma)	2σ (Ma)	YC2σ(3+) (Ma)	2σ (Ma)	MLA (Ma)	2σ (Ma)	CAYP (Ma)	2σ (Ma)	Preferred MDA					
Bat Mountain	Bat Mountain Fm	Sandstone mbr	N_10-22-98-1	Tuff	Ar/Ar	Sanidine	–	–	–	–	–	–	–	–	–	–	–	–	13.52	0.07	13.52	0.07	Fridrich et al. (2012)
Bat Mountain	Bat Mountain Fm	Sandstone mbr	21TMS013	Tuff	U-Pb	Zircon	15.0	14.39	0.66	14.60	0.16	14.80	0.10	15.00	0.05	15.07	0.06	MLA	–	–	15.00	0.05	This study
Bat Mountain	Bat Mountain Fm	Conglomerate mbr	21TMS011	Sandstone	U-Pb	Zircon	15.0	14.90	0.40	15.00	0.24	15.09	0.22	15.30	0.15	15.33	0.18	MLA	–	–	15.30	0.15	This study
Bat Mountain	Amargosa Valley Fm	Red sandstone mbr	21TMS010	Sandstone	U-Pb	Zircon	21.0	18.10	0.59	19.45	0.28	19.84	0.21	18.49	0.36	21.73	0.22	MLA	–	–	18.49	0.36	This study
Bat Mountain	Amargosa Valley Fm	Red sandstone mbr	None given	Tuff	K/Ar	Biotite	–	–	–	–	–	–	–	–	–	–	–	–	19.80	0.20	19.80	0.20	Çemen et al. (1985)
Bat Mountain	Amargosa Valley Fm	Red sandstone mbr	11-9-00-1	Tuff	Ar/Ar	Sanidine	–	–	–	–	–	–	–	–	–	–	–	–	21.58	0.16	21.58	0.16	Fridrich et al. (2012)
Bat Mountain	Amargosa Valley Fm	Red sandstone mbr	21TMS007	Sandstone	U-Pb	Zircon	23.0	21.73	0.40	21.88	0.32	22.21	0.22	22.79	0.19	23.13	0.21	MLA	–	–	22.79	0.19	This study
Bat Mountain	Amargosa Valley Fm	Limestone mbr	M_10-21-98-1	Tuff	Ar/Ar	Sanidine	–	–	–	–	–	–	–	–	–	–	–	–	22.57	0.10	22.57	0.10	Fridrich et al. (2012)
Bat Mountain	Amargosa Valley Fm	Limestone mbr	21TMS005	Tuff	U-Pb	Zircon	24.0	22.91	0.80	23.30	0.22	23.50	0.16	23.79	0.06	24.27	0.39	MLA	–	–	23.79	0.06	This study
Bat Mountain	Amargosa Valley Fm	Limestone mbr	21TMS004	Tuff	U-Pb	Zircon	25.0	23.86	0.76	24.40	0.18	24.60	0.14	24.65	0.07	24.97	0.18	MLA	–	–	24.65	0.07	This study
Bat Mountain	Amargosa Valley Fm	Limestone mbr	21TMS002	Tuff	U-Pb	Zircon	25	24.13	0.41	24.30	0.10	24.50	0.06	24.65	0.06	24.65	0.06	MLA	–	–	24.65	0.06	This study
Bat Mountain	Amargosa Valley Fm	Limestone mbr	None given	Tuff	K/Ar	Biotite	–	–	–	–	–	–	–	–	–	–	–	–	24.70	0.30	24.70	0.30	Çemen et al. (1985)
Bat Mountain	Amargosa Valley Fm	Limestone mbr	21TMS003	Tuff	U-Pb	Zircon	26.0	25.32	0.64	25.60	0.14	25.90	0.08	25.87	0.04	25.91	0.04	MLA	–	–	25.87	0.04	This study
Bat Mountain	Amargosa Valley Fm	Conglomerate mbr	21TMS009	Sandstone	U-Pb	Zircon	26.0	24.64	1.37	25.27	0.34	25.64	0.24	26.26	0.22	26.30	0.23	MLA	–	–	26.26	0.22	This study
Bat Mountain	Amargosa Valley Fm	Conglomerate mbr	21TMS001	Sandstone	U-Pb	Zircon	28.0	26.56	1.25	27.26	0.30	27.68	0.25	28.34	0.24	28.73	0.26	MLA	–	–	28.34	0.24	This study
Titus Canyon	Wahguyhe Fm	Undivided	ELM18DVTC-12	Marl, ashy	U-Pb	Zircon	16.0	13.84	2.08	14.40	0.37	14.70	0.30	14.51	0.38	14.68	0.21	MLA	–	–	14.51	0.38	Miller et al. (2022)
Titus Canyon	Panuga Fm	Undivided	TC-10	Tuff	Ar/Ar	Sanidine	–	–	–	–	–	–	–	–	–	–	–	–	12.10	0.20	12.10	0.20	Midttun (2022)
Titus Canyon	Panuga Fm	Undivided	*ELM18DVTC-10	Tuff	U-Pb	Zircon	15	9.60	0.10	10.90	0.08	12.40	0.08	9.60	0.10	15.00	0.19	CAYP	–	–	15.00	0.19	Miller et al. (2022)
Titus Canyon	Panuga Fm	Undivided	592-GV1_K1	Tuff	Ar/Ar	Sanidine	–	–	–	–	–	–	–	–	–	–	–	–	15.70	0.20	15.70	0.20	Snow and Lux (1999)
Titus Canyon	Titus Canyon Fm	Variegated mbr	ELM18DVTC-7	Sandstone	U-Pb	Zircon	25.0	18.77	0.20	22.70	0.23	22.80	0.22	18.77	0.05	24.53	0.06	CAYP	–	–	24.53	0.06	Miller et al. (2022)
Titus Canyon	Titus Canyon Fm	Variegated mbr	TC-4	Tuff	Ar/Ar	Biotite	–	–	–	–	–	–	–	–	–	–	–	–	30.20	1.20	30.20	1.20	Saylor and Hodges (1994)
Titus Canyon	Titus Canyon Fm	Variegated mbr	*TC-09-04	Sandstone	U-Pb	Zircon	34.0	30.91	4.23	32.30	1.06	33.30	0.44	33.91	0.19	33.99	0.38	MLA	–	–	33.91	0.19	Midttun (2022)
Titus Canyon	Titus Canyon Fm	Variegated mbr	Unit_38_tuff	Tuff	U-Pb	Zircon	33.0	24.03	0.65	30.60	0.57	30.80	0.52	24.03	0.55	32.89	0.39	CAYP	–	–	32.89	0.39	Midttun (2022)
Titus Canyon	Titus Canyon Fm	Variegated mbr	ELM18DVTC-6	Sandstone	U-Pb	Zircon	34.0	29.95	0.44	31.80	0.29	32.10	0.29	29.95	0.30	33.34	0.47	CAYP	–	–	33.34	0.47	Miller et al. (2022)
Titus Canyon	Titus Canyon Fm	Variegated mbr	TC19-9	Tuff	U-Pb	Zircon	35.0	32.83	0.71	33.10	0.48	33.70	0.38	34.85	0.34	35.50	0.37	MLA	–	–	34.85	0.34	Midttun (2022)
Titus Canyon	Titus Canyon Fm	Variegated mbr	T1	Tuff	Ar/Ar	Biotite	–	–	–	–	–	–	–	–	–	–	–	–	34.50	0.80	34.50	0.80	Saylor and Hodges (1994)
Titus Canyon	Titus Canyon Fm	Variegated mbr	ELM18DVTC-2	Sandstone	U-Pb	Zircon	35.0	25.87	0.26	30.80	0.42	30.90	0.41	25.87	0.34	35.00	0.45	CAYP	–	–	35.00	0.45	Miller et al. (2022)
Titus Canyon	Titus Canyon Fm	Variegated mbr	TC19-2	Sandstone	U-Pb	Zircon	36.0	34.70	0.99	35.30	0.56	35.70	0.44	36.17	0.35	36.23	0.38	MLA	–	–	36.17	0.35	Midttun (2022)
Titus Canyon	Titus Canyon Fm	Variegated mbr	ELM18DVTC-1	Sandstone	U-Pb	Zircon	37.0	36.27	0.36	89.30	0.71	157.20	1.14	36.74	0.25	36.84	0.44	MLA	–	–	36.74	0.25	Miller et al. (2022)
Boundary Canyon fault klippe	Titus Canyon Fm equivalent	Undivided	MR19DV-4	Sandstone	U-Pb	Zircon	25.0	21.58	0.25	22.20	0.19	23.20	0.18	21.58	0.18	24.76	0.16	MLA	–	–	21.58	0.18	Miller et al. (2022)
Boundary Canyon fault klippe	Titus Canyon Fm equivalent	Undivided	MR19DV-5	Tuff	U-Pb	Zircon	23.0	20.08	7.21	23.50	1.07	23.50	1.07	23.58	0.47	23.58	0.56	MLA	–	–	23.58	0.47	Miller et al. (2022)
Boundary Canyon fault klippe	Titus Canyon Fm equivalent	Undivided	MR19DV-8	Sandstone	U-Pb	Zircon	26.0	20.79	0.22	22.80	0.22	22.90	0.21	20.79	0.18	25.64	0.22	CAYP	–	–	25.64	0.22	Miller et al. (2022)
Boundary Canyon fault klippe	Titus Canyon Fm equivalent	Undivided	MR19DV-3	Tuff	U-Pb	Zircon	34.0	32.76	2.06	33.70	0.70	34.10	0.56	34.09	0.37	34.09	0.37	MLA	–	–	34.09	0.37	Miller et al. (2022)
Monarch Canyon–Keane Spring area	Titus Canyon Fm	Undivided	ELM15MC-12	Sandstone	U-Pb	Zircon	35.0	32.20	4.26	33.50	0.62	34.20	0.51	34.18	0.39	34.19	0.39	MLA	–	–	34.18	0.39	Miller et al. (2022)
Monarch Canyon–Keane Spring area	Titus Canyon Fm	Undivided	ELM15MC-11	Sandstone	U-Pb	Zircon	35.0	33.45	2.69	34.00	1.88	36.00	0.39	36.01	0.34	36.01	0.34	MLA	–	–	36.01	0.34	Miller et al. (2022)
Indian Butte area	Rocks of Porter Mine	Undivided	FM-2_16-5	Tuff	Ar/Ar	Biotite	–	–	–	–	–	–	–	–	–	–	–	–	19.30	0.50	19.30	0.50	Murray (2002); Gutenkunst (2006)
Indian Butte area	Rocks of Porter Mine	Undivided	FM-3_102-5	Tuff	Ar/Ar	Sanidine	–	–	–	–	–	–	–	–	–	–	–	–	23.60	0.10	23.60	0.10	Murray (2002); Gutenkunst (2006)
Indian Butte area	Rocks of Porter Mine	Undivided	FM-3_2-1	Tuff	Ar/Ar	Biotite	–	–	–	–	–	–	–	–	–	–	–	–	28.20	0.20	28.20	0.20	Murray (2002); Gutenkunst (2006)
Furnace Creek Area	Funeral Fm	Undivided	None given	Basalt	K/Ar	Whole rock	–	–	–	–	–	–	–	–	–	–	–	–	4.03	0.12	4.03	0.12	Çemen et al. (1985)
Furnace Creek Area	Furnace Creek Fm	Undivided	None given	Basalt	K/Ar	Biotite	–	–	–	–	–	–	–	–	–	–	–	–	5.87	1.50	5.87	1.50	Çemen et al. (1985)
Furnace Creek Area	Artist Drive Fm	Undivided	G_11-18-99-8	Tuff	Ar/Ar	Sanidine	–	–	–	–	–	–	–	–	–	–	–	–	8.93	0.06	8.93	0.06	Fridrich et al. (2012)
Ryan-Billie Mine	Artist Drive Fm	Upper pyroclastic mbr	None given	Tuff	K/Ar	Biotite	–	–	–	–	–	–	–	–	–	–	–	–	6.40	0.30	6.40	0.30	Çemen et al. (1985)
Ryan-Billie Mine	Artist Drive Fm	Lower pyroclastic mbr	None given	Tuff	K/Ar	Biotite	–	–	–	–	–	–	–	–	–	–	–	–	10.60	0.20	10.60	0.20	Çemen et al. (1985)
Ryan-Billie Mine	Artist Drive Fm	Lower sedimentary mbr	None given	Tuff	K/Ar	Biotite	–	–	–	–	–	–	–	–	–	–	–	–	12.70	0.40	12.70	0.40	Çemen et al. (1985)
Ryan-Billie Mine	Artist Drive Fm	Lower sedimentary mbr	I_3-23-00-3	Tuff	Ar/Ar	Sanidine	–	–	–	–	–	–	–	–	–	–	–	–	13.20	0.06	13.20	0.06	Fridrich et al. (2012)
Ryan-Billie Mine	Artist Drive Fm	Lower sedimentary mbr	None given	Tuff	K/Ar	Biotite	–	–	–	–	–	–	–	–	–	–	–	–	13.70	0.40	13.70	0.40	Çemen et al. (1985)
Eagle Mountain	Eagle Mountain Fm	Member 3 (lacustrine)	EM-4	Tuff	Ar/Ar	Sanidine	–	–	–	–	–	–	–	–	–	–	–	–	11.63	0.32	11.63	0.32	Niemi et al. (2001)
Eagle Mountain	Eagle Mountain Fm	Member 2 (fluvial)	*EM-1	Sandstone	U-Pb	Zircon	n/a	11.10	2.20	97.90	3.98	171.60	1.66	11.10	1.10	17.69	5.69	YSG, MLA	–	–	11.10	2.20	Niemi (2012)
Eagle Mountain	Eagle Mountain Fm	Member 2 (fluvial)	*EM-2	Sandstone	U-Pb	Zircon	14.0	11.10	2.00	12.30	1.12	14.10	0.34	14.06	0.18	13.93	0.56	MLA	–	–	14.06	0.18	Niemi (2012)
Eagle Mountain	Eagle Mountain Fm	Member 1 (breccia clast)	EM-0	Tuff	Ar/Ar	Sanidine	–	–	–	–	–	–	–	–	–	–	–	–	13.35	0.47	13.35	0.47	Niemi et al. (2001)

Note: Fm—Formation; mbr—member; CAYP—central age of youngest peak; MDA—maximum depositional age; MLA—maximum likelihood age; YSG—youngest single grain; YPP—youngest graphical peak. Dash (–) indicates that a given metric or age is not applicable.

*Samples notated with an asterisk (*) are characterized by MDAs calculated with analytical uncertainty only due to a lack of information regarding external errors.

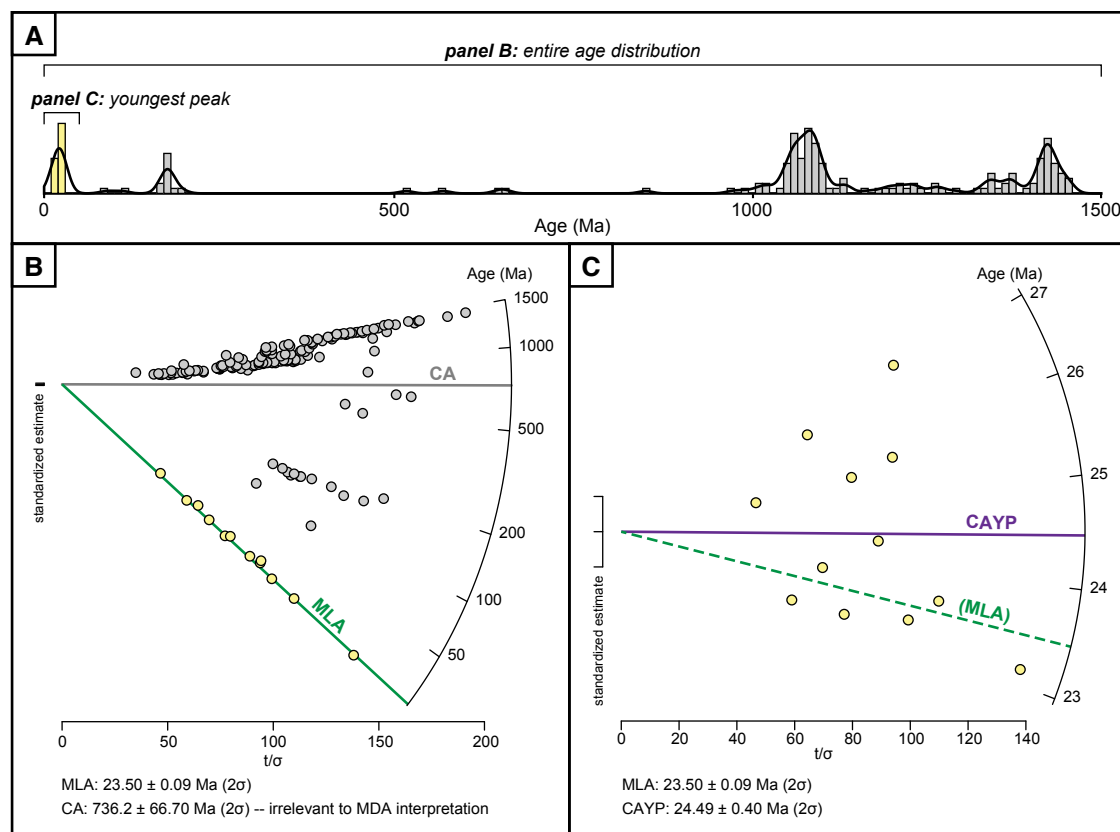**2σ uncertainties associated with ⁴⁰Ar/³⁹Ar and K/Ar dates are presumed to include only analytical error.

Figure 5. Conceptual diagram showing the differences between the maximum likelihood age (MLA) as described by Vermeesch (2021) and the central age of the youngest peak (CAYP) variant applied in this study. (A) Hypothetical detrital zircon distribution characterized by many age peaks, including one discrete Cenozoic peak. (B) Radial plot generated using all detrital ages as inputs, with the MLA shown in green and a central age (CA) that is irrelevant to the depositional age of the sample. (C) A modified radial plot generated using only the detrital ages that comprise the youngest peak, with a CAYP shown in purple and the MLA of the entire distribution shown in green for reference. MDA—maximum depositional age.

indicating minor post-depositional reworking by currents. Concordant dates were acquired for 42 zircon grains, with 40 dates ranging from ca. 29 Ma to 24 Ma and two dates >1.0 Ga (Table S1, see footnote 1). Cenozoic zircon dates yield a WMA of 24.62 ± 0.07 Ma (2σ; n = 36/42) and a MLA of 24.65 ± 0.07 Ma (2σ; n = 40/42) (Table 2; Fig. 6B).

21TMS005: Upper Part of the Limestone Member, Amargosa Valley Formation

Sample 21TMS005 was collected from a bright white, 20-m-thick tuff in the upper part of the limestone member of the Amargosa Valley Formation, ~15 m up-section from sample 21TMS004 and ~40 m below the lithostratigraphic top of the limestone member as mapped herein (Figs. 3 and 4A). The tuff directly overlies a gray, indurated but structureless limestone bed. The basal 20–30 cm of the tuffaceous interval consist of bright green, crystal-rich and grain-supported, medium-grained volcaniclastic sandstone that displays crude lamination and contains the casts of palm fronds. The remainder of the tuff interval is bright white, ash-dominated, and fines upward from fine- to very fine-grained. The fine-grained portion of the tuff contains phenocrysts and small, slightly flattened pumice clasts that become less common upward; sample 21TMS005 was collected from the lower part of the pumice-bearing horizon. Phenocrysts include sanidine, plagioclase, biotite, and euhedral to anhedral quartz in a devitrified siliceous matrix. The upper few meters of the tuff display soft-sediment deformation (including flame structures) and planar lamination, with the planar-laminated interval altered to vibrant purple, red, and orange colors. The tuff is abruptly overlain by an ~10-m-thick succession of volcaniclastic sandstone that contains abundant current ripples, low-angle planar lamination, and upper flow regime structures, which is in turn overlain by ~10 m of limestone. The presence of limestone beds above and below the
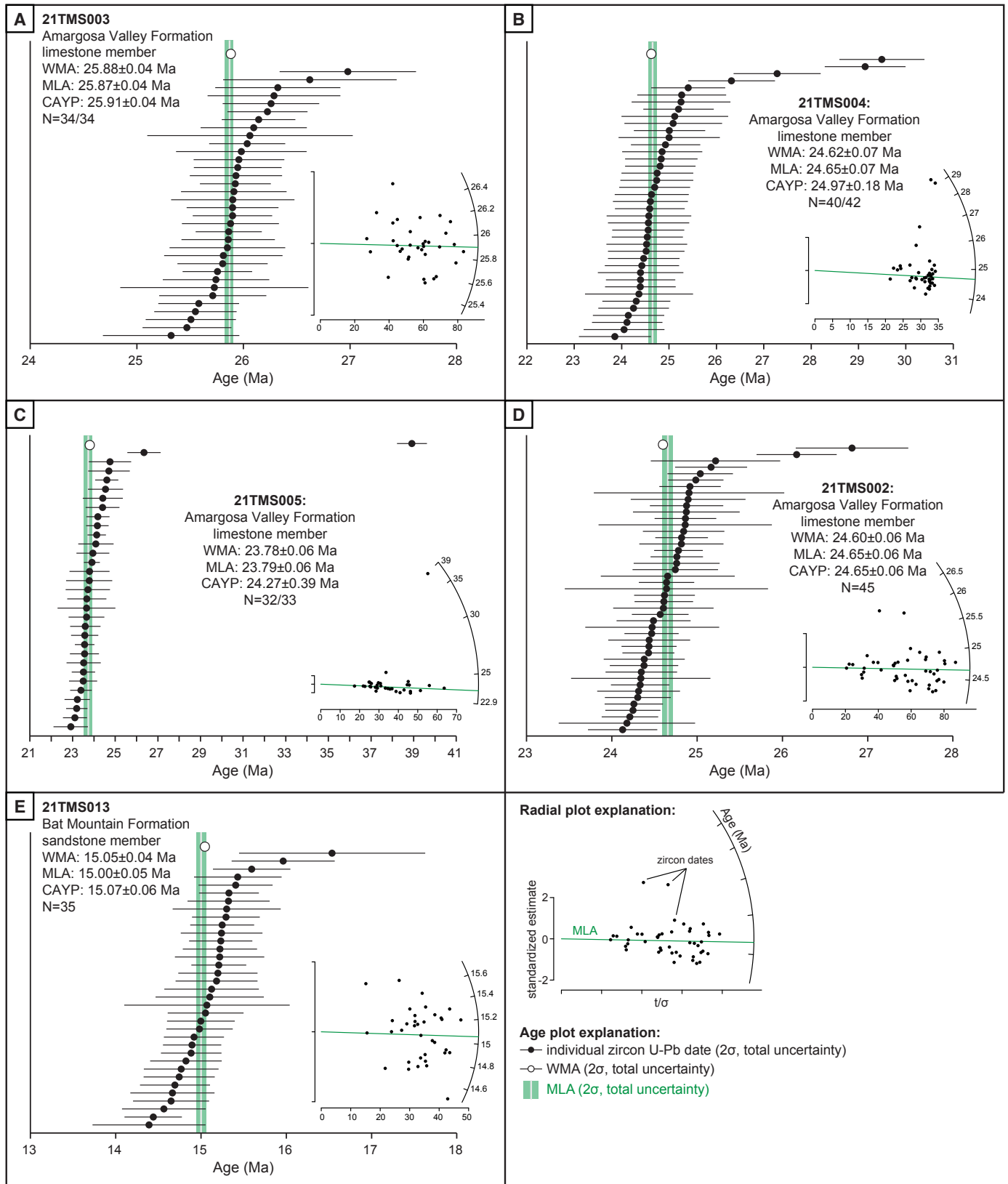
Figure 6. Plots of zircon ages of tuff samples from the Amargosa Valley and Bat Mountain formations showing both individual zircon dates (at 2σ and including both analytical and systematic uncertainty) and interpreted depositional/eruptive ages (at 2σ and including both analytical and systematic uncertainty) based on the maximum likelihood age (MLA) metric. (A) Sample 21TMS003 from the limestone member of the Amargosa Valley Formation. (B) Sample 21TMS004 from the limestone member of the Amargosa Valley Formation. (C) Sample 21TMS005 from the limestone member of the Amargosa Valley Formation. (D) Sample 21TMS002 from what was originally mapped as the red sandstone member of the Amargosa Valley Formation (Fridrich et al., 2012) but is redefined herein as the limestone member of the Amargosa Valley Formation. (E) Sample 21TMS013 from the sandstone member of the Bat Mountain Formation. Abbreviations: CAYP—central age of the youngest peak; WMA—weighted mean age.

entire tuffaceous interval, paired with the presence of volcaniclastic sediments containing current structures, suggest deposition in a marginal lacustrine setting vulnerable to transient, relatively high-energy currents. Concordant dates were acquired for 33 zircon grains, with 31 dates ranging from ca. 26 Ma to 23 Ma, one date of ca. 39 Ma, and one date >1.0 Ga (Table S1, see footnote 1). Cenozoic zircon dates yield a WMA of 23.78 ± 0.06 Ma (2σ; n = 30/33) and a MLA of 23.79 ± 0.06 Ma (2σ; n = 32/33) (Table 2; Fig. 6C).

21TMS002: Amargosa Valley Formation

Sample 21TMS002 was collected from a pale green tuff at what was previously mapped by Fridrich et al. (2012) as the lithostratigraphic top of the red sandstone member of the Titus Canyon Formation (Amargosa Valley Formation herein), which is exposed directly beneath the prominent base of the Kelley's Well Limestone (Fig. 3). The tuff is ~3 m thick, well-exposed, and pervasively fractured. In hand sample, the tuff is characterized by obvious quartz, sanidine, and biotite phenocrysts in a siliceous, ashy matrix. Lithic grains are also present but compose <10% of the observed grains. Concordant dates were acquired for 45 zircon grains, ranging from ca. 24 Ma to 27 Ma (Table S1, see footnote 1). Cenozoic zircon dates yield a WMA of 24.60 ± 0.06 Ma (2σ; n = 43/45) and a MLA of 24.65 ± 0.06 Ma (2σ; n = 45/45) (Table 2; Fig. 6D). Notably, the MLA is indistinguishable at 95% confidence from the MLA of sample 21TMS004 (24.65 ± 0.07 Ma, 2σ) from the limestone member of the Amargosa Valley Formation. For this reason, we interpret that sample 21TMS002 was collected from a small, fault-bounded exposure of the limestone member of the Amargosa Valley Formation that was previously unrecognized by Fridrich et al. (2012).

21TMS013: Middle Part of the Sandstone Member, Bat Mountain Formation

Sample 21TMS013 was collected from a bright white tuff in the approximate middle of the exposed part of the sandstone member of the Bat Mountain Formation (Fig. 3). The tuff is ~3 m thick and is very poorly exposed in a recessive interval; it is bounded by an ~20-m-thick conglomeratic interval below and an ~10-m-thick pebbly sandstone interval above. Phenocrysts include quartz, plagioclase, and sanidine in a very fine-grained siliceous ash matrix. Concordant dates were acquired for 35 zircon grains, ranging from ca. 14 Ma to 16 Ma (Table S1, see footnote 1). Cenozoic zircon dates yield a WMA of 15.05 ± 0.04 Ma (2σ; n = 35/35) and a MLA of 15.00 ± 0.05 Ma (2σ; n = 35/35) (Table 2; Fig. 6E).

Detrital Zircon U-Pb Geochronology

Five sandstone samples from the Amargosa Valley and Bat Mountain formations yielded detrital zircon dates ranging from Archean to Miocene that are present in variable proportions across the samples (Fig. 7). Prominent age groups reflect a combination of first-cycle derivation from crystalline sources and recycling from sedimentary sources of zircon (e.g., Schwartz et al., 2019): Cenozoic and Mesozoic dates respectively reflect contributions from Cenozoic volcanic fields of the Great Basin and erosion of Mesozoic plutons associated with the Sierran arc, whereas dates >500 Ma most likely reflect the recycling of grains from Neoproterozoic and Paleozoic strata that are widely exposed across the region. Notably, the abundant Cenozoic ages present in all samples (Fig. 7) help constrain the depositional age of each unit sampled (Fig. 8).

21TMS001 and 21TMS009: Conglomerate Member, Amargosa Valley Formation

Samples 21TMS001 and 21TMS009 were respectively collected from the lower and upper parts of the conglomerate member of the Amargosa Valley Formation. Sample 21TMS001 was collected ~15 m above the lithostratigraphic base of the unit (Fig. 3) from the red, silty sandstone matrix of a structureless and poorly bedded cobble conglomerate (Fig. 4C). At this horizon, clasts are dominantly Paleozoic limestone with minor white quartzite. Sample 21TMS009 was collected ~25 m below the lithostratigraphic top of the unit (Figs. 3 and 4A) from a reddish sandstone lens bound by crudely bedded cobble conglomerate. Clasts in the upper part of the unit are a relatively even mix of Paleozoic limestone and quartzite.

Both samples yielded Cenozoic (44–48%), Mesozoic (dominantly Early–Middle Jurassic; 29–34%), Paleozoic (1%), and Proterozoic dates (30–35%; Fig. 7; Table S2, see footnote 1). More than 100 Cenozoic dates in each sample form near-normal distributions with few outliers (Figs. 8A and 8B). MDAs calculated for sample 21TMS001 range from 26.56 ± 1.25 Ma (2σ; YSG) to 28.73 ± 0.26 Ma (2σ; CAYP), whereas MDAs for sample 21TMS009 range from 24.64 ± 1.37 Ma (2σ; YSG) to 26.30 ± 0.23 Ma (2σ; CAYP) (Table 2). For both samples, we interpret the MLA metric to best approximate depositional age, bracketing deposition of the conglomerate member of the Amargosa Valley Formation between 28.34 ± 0.24 Ma (2σ; 21TMS001) and 26.26 ± 0.22 Ma (2σ; 21TMS009).

21TMS007 and 21TMS010: Red Sandstone Member, Amargosa Valley Formation

Samples 21TMS007 and 21TMS010 were respectively collected from the base and top of the red sandstone member of the Amargosa Valley Formation. Sample 21TMS007 was collected from the first prominent sandstone unit that overlies the recessive limestone member of the Amargosa Valley Formation, the horizon used herein to demarcate the lithostratigraphic base of the red sandstone member (Figs. 3 and 4A). The sampled unit is conglomeratic at its base and fines upward to medium-grained sandstone. Sample 21TMS010 was collected from ~20 m below the contact between the red sandstone member
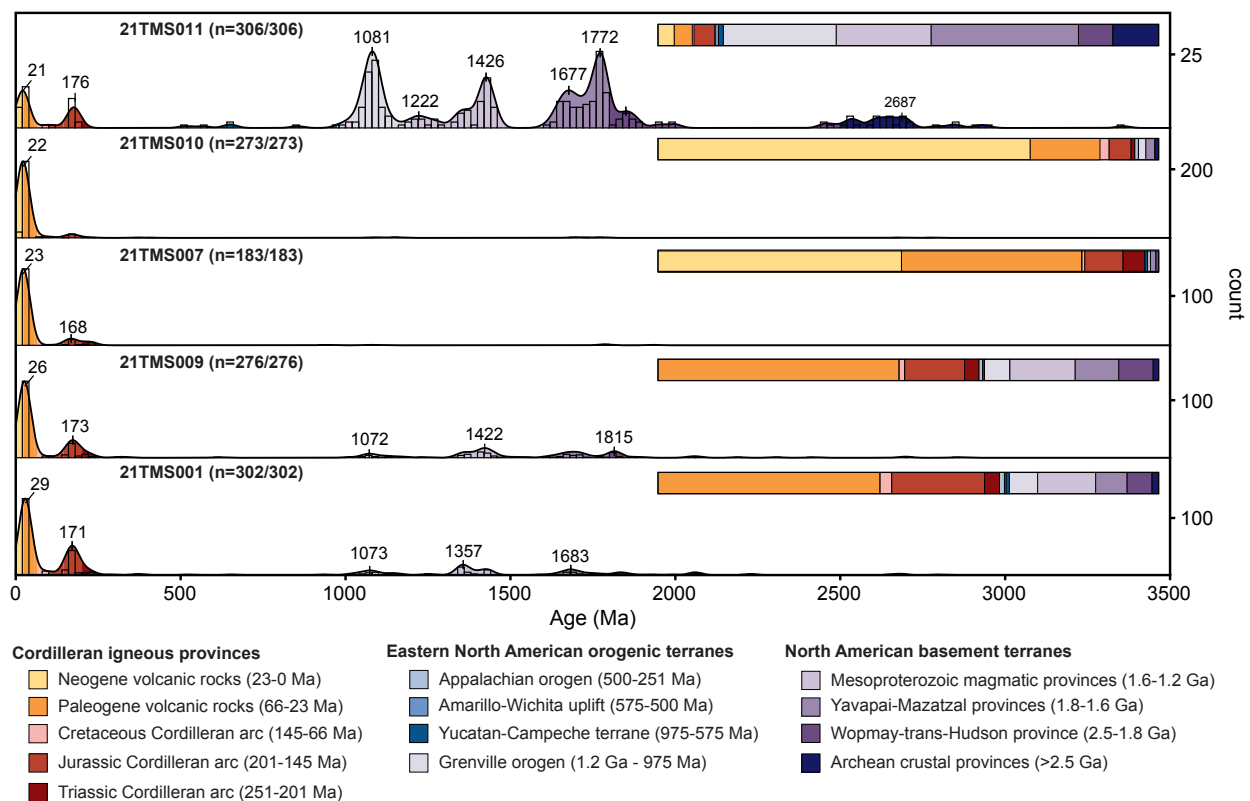
Cordilleran igneous provinces
- ▢ Neogene volcanic rocks (23-0 Ma)
- ▢ Paleogene volcanic rocks (66-23 Ma)
- ▢ Cretaceous Cordilleran arc (145-66 Ma)
- ▢ Jurassic Cordilleran arc (201-145 Ma)
- ▢ Triassic Cordilleran arc (251-201 Ma)

Eastern North American orogenic terranes
- ▢ Appalachian orogen (500-251 Ma)
- ▢ Amarillo-Wichita uplift (575-500 Ma)
- ▢ Yucatan-Campeche terrane (975-575 Ma)
- ▢ Grenville orogen (1.2 Ga - 975 Ma)

North American basement terranes
- ▢ Mesoproterozoic magmatic provinces (1.6-1.2 Ga)
- ▢ Yavapai-Mazatzal provinces (1.8-1.6 Ga)
- ▢ Wopmay-trans-Hudson province (2.5-1.8 Ga)
- ▢ Archean crustal provinces (>2.5 Ga)

Figure 7. Kernel density estimates (KDEs) and stacked histograms for detrital zircon samples from the Amargosa Valley and Bat Mountain formations (KDE bandwidth = 20; histogram bin width = 20 Ma). Plots are arranged stratigraphically, with the lowest sample on the bottom. Color-coded age intervals are adapted from Schwartz et al. (2019) and references within.

and the overlying Kelley's Well Limestone (Fig. 3). At this horizon, sandstone beds are medium- to coarse-grained and broadly lenticular, separated by thin mudstone interbeds.

Both samples are dominated by Cenozoic zircon dates (85–88%) with minor Mesozoic (7–13%), Paleozoic (0–1%), and Proterozoic dates (3–4%; Fig. 7; Table S2, see footnote 1). In both samples, Cenozoic grains form near-normal distributions with positively skewed tails (Figs. 8C and 8D). More than 150 Cenozoic zircon dates yield MDAs ranging from 21.73 ± 0.40 Ma (2σ; YSG) to 23.13 ± 0.21 Ma (2σ; CAYP) for sample 21TMS007, whereas more than 200 Cenozoic zircon dates yield MDAs ranging from 18.10 ± 0.59 Ma (2σ; YSG) to 21.73 ± 0.22 Ma (2σ; CAYP) for sample 21TMS010 (Table 2). For both samples, we interpret the MLA metric to best approximate depositional age, bracketing deposition of the red sandstone member of the Amargosa Valley Formation between 22.79 ± 0.19 Ma (2σ; 21TMS007) and 18.49 ± 0.36 Ma (2σ; 21TMS010).

21TMS011: Conglomerate Member, Bat Mountain Formation

Sample 21TMS011 was collected from the lower part of the conglomerate member of the Bat Mountain Formation, ~20 m above the base of the unit (Figs. 3 and 4B). This sample was collected from a tan, silty sandstone lens bound by beds of pebble to cobble conglomerate (Fig. 4E). Internally, the sandstone lens contained crude, soft sediment-deformed laminations.

Compared to samples from underlying units, sample 21TMS011 contains relatively few Cenozoic zircon dates (7%; Fig. 7; Table S2, see footnote 1). The sample also contains few Mesozoic (5%) and Paleozoic (1%) dates and is instead overwhelmed by Proterozoic dates (88%; Fig. 7; Table S2). Unlike those in lower samples, Cenozoic grains form a bimodal distribution with peaks at ca. 15 Ma and 24 Ma (Fig. 8E). Twenty-one Cenozoic zircon dates yield MDAs ranging from 14.90 ± 0.40 Ma (2σ; YSG) to 15.33 ± 0.18 Ma (2σ; CAYP) (Table 2).
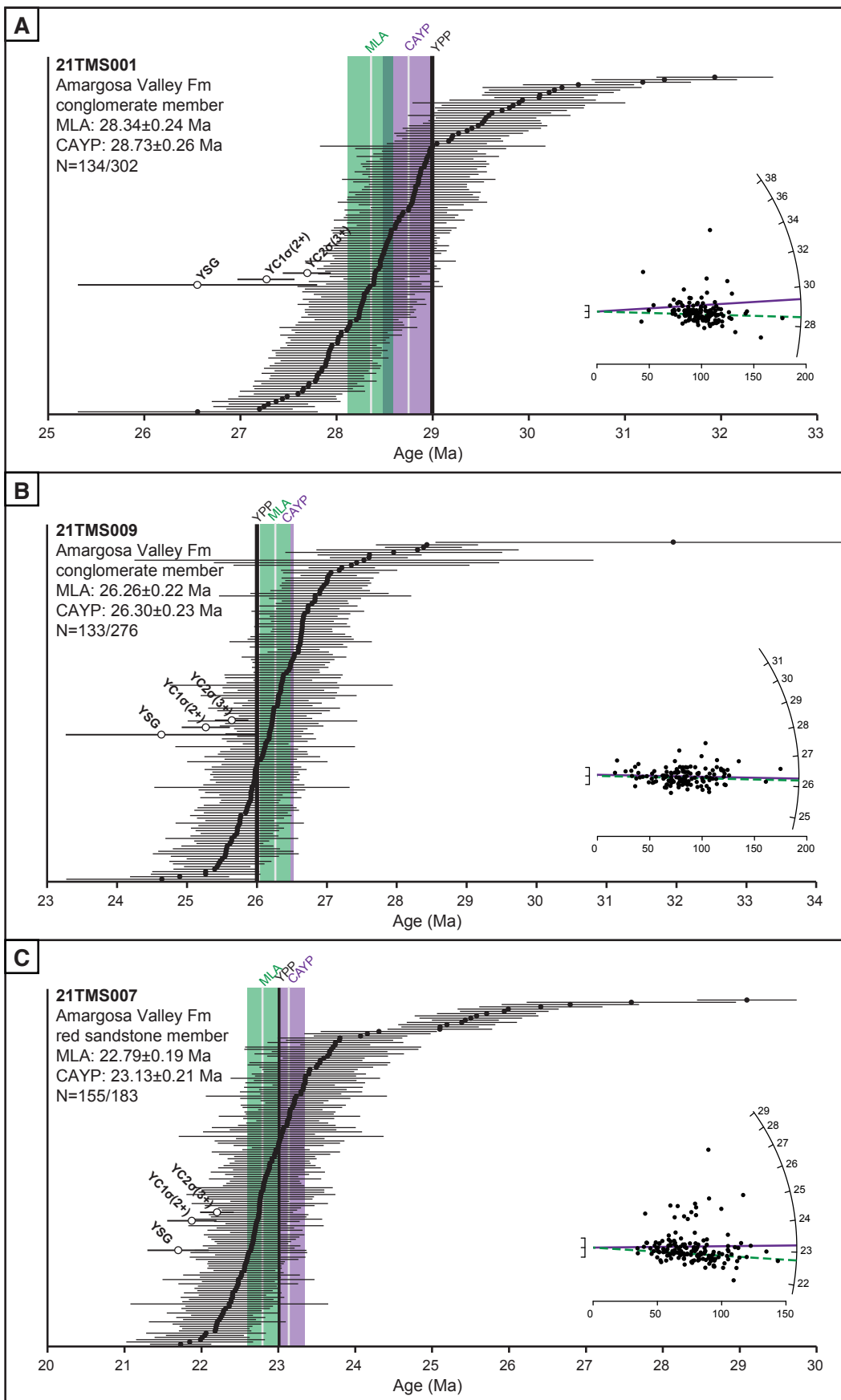
Figure 8. Detrital zircon distributions for sandstone samples from the Amargosa Valley and Bat Mountain formations showing both individual zircon dates (at 2σ and including only analytical uncertainty) and maximum depositional ages (MDAs; at 2σ and including both analytical and systematic uncertainty) interpreted using the maximum likelihood age (MLA) and central age of the youngest peak (CAYP) metrics. Other commonly used MDAs are shown for comparison. (A) Sample 21TMS001 from the conglomerate member of the Amargosa Valley Formation. (B) Sample 21TMS009 from the conglomerate member of the Amargosa Valley Formation. (C) Sample 21TMS007 from the red sandstone member of the Amargosa Valley Formation. (*Continued on following page.*)
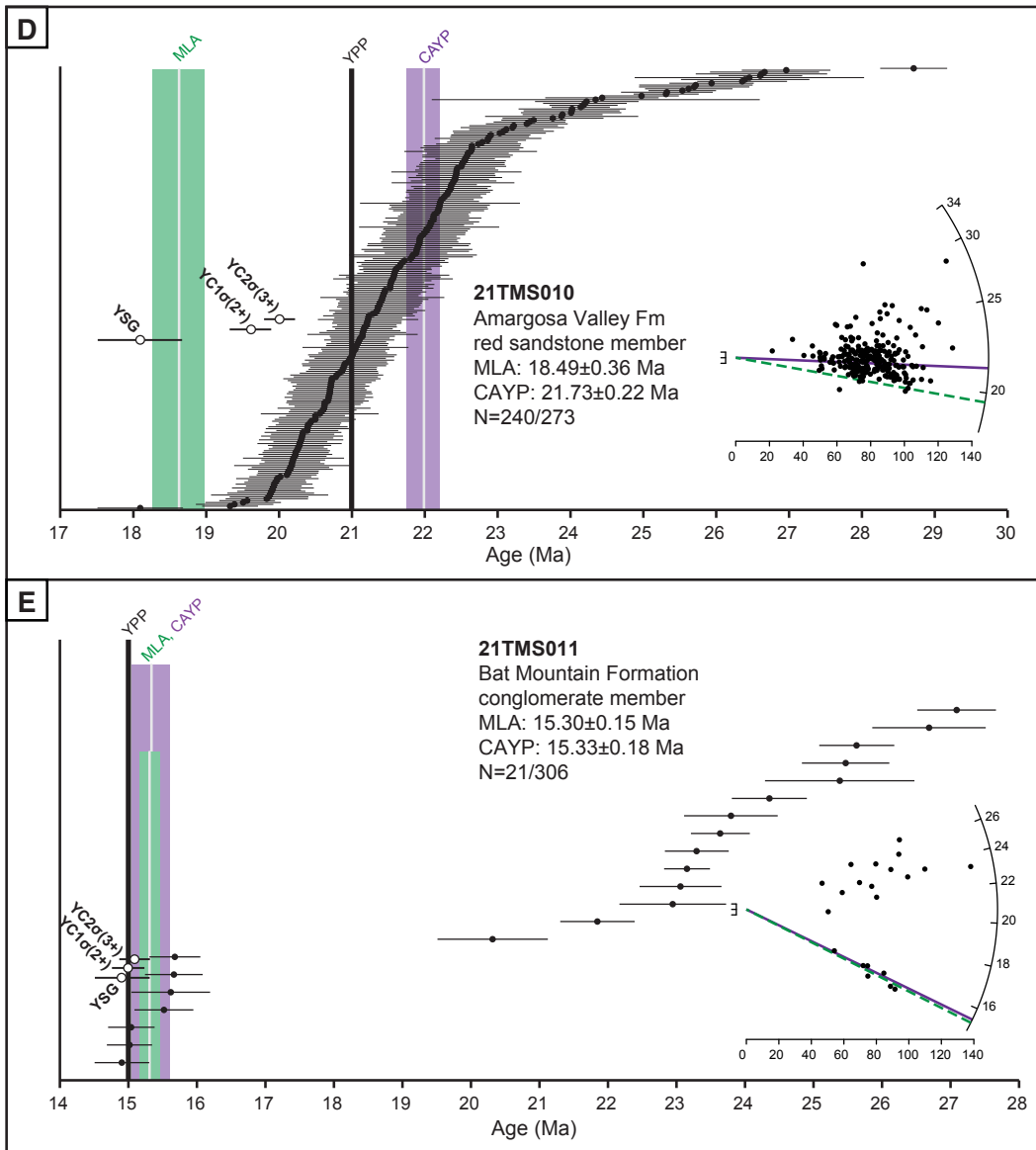
Figure 8 (*continued*). (D) Sample 21TMS010 from the red sandstone member of the Amargosa Valley Formation. (E) Sample 21TMS011 from the conglomerate member of the Bat Mountain Formation. Abbreviations: YC1σ(2+)—weighted mean of the youngest grain cluster overlapping at 1σ standard error; YC2σ(3+)—weighted mean of the youngest grain cluster overlapping at 2σ standard error; YPP—youngest graphical peak; YSG—youngest single grain.
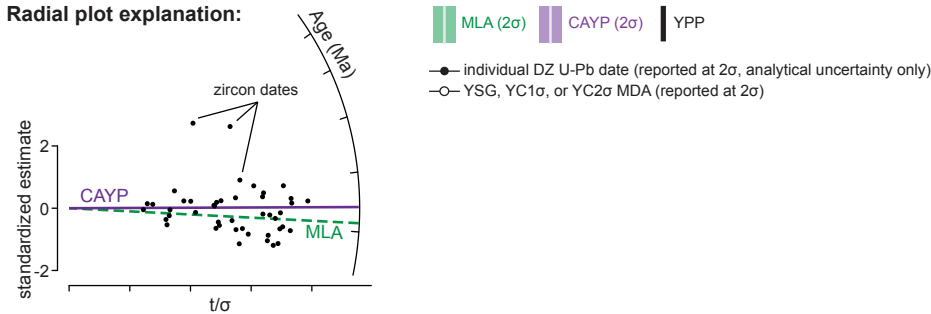
We interpret the MLA metric to best approximate depositional age, providing a lower bound on the depositional age of the conglomerate member of the Bat Mountain Formation of 15.30 ± 0.15 Ma (2σ).

■ DISCUSSION

MDAs from Zircon U-Pb data: An Argument for the MLA Metric

With few exceptions, we adopt the MLA metric as our preferred MDA for both new and compiled tuff and sandstone samples discussed herein. Recent studies have shown that MDA estimates using more ad hoc approaches either tend to drift toward unreasonably young—e.g., YSG, YC1σ(2+), YC2σ(3+)—or old (e.g., YPP) values as the number of young ages measured within a sample increases (Coutts et al., 2019; Johnstone et al., 2019; Sharman and Malkowski, 2020). The YSG metric inherently omits consideration of all older dates in a distribution, and especially for samples characterized by a large number of young grains, the YC1σ(2+) and YC2σ(3+) metrics preferentially utilize the dates on the young tail of a distribution. In contrast, the MLA metric is derived from convergence of a minimum age model to a unique value without the need to ignore any young (or old) dates in an age distribution (Galbraith and Laslett, 1993; Vermeesch, 2021). Below, we provide an argument for systematic use of the MLA metric and its variant, the CAYP, with comments on both advantages and disadvantages of the method.

Table 2 compares commonly used MDA metrics for both new and published detrital zircon samples. Depending on the spread of young ages considered for each sample, there may be millions of years of difference between the YSG and other MDA metrics. Figure 9 is a graphical representation of the degree of such variability for two end-member examples: an unnamed tuff from the limestone member of the Amargosa Valley Formation (sample 21TMS004; Figs. 9A–9C; this study) and the Crystal Marker Tuff (Reynolds, 1969) of the Panuga Formation, where it is exposed at Titus Canyon (ELM18DVTC-10; Figs. 9D–9F, with data shown as originally discussed in Miller et al., 2022).

Sample 21TMS004 yielded 40 Cenozoic zircon dates that are tightly clustered around 25 Ma, with a few outliers that extend to ca. 30 Ma (Fig. 9A) and two dates >1.0 Ga. The Cenozoic age distribution is characteristic of a volcanic eruptive cycle with mostly syn-eruptive ages and a positively skewed tail of pre-eruptive xenocryst ages (after Vermeesch, 2021). In this "well behaved" example, the various MDA metrics yield ages that are indistinguishable from one another (i.e., they overlap at 2σ uncertainty) (Fig. 9A). In this case, the YC1σ(2+), YC2σ(3+), MLA, or CAYP could each be justified as a reasonable MDA for the sample.

In contrast, sample ELM18DVTC-10 yielded 143 Cenozoic zircon dates that are broadly distributed around 15 Ma, with skewed tails extending to ca. 19 Ma and ca. 9.5 Ma (Fig. 9D). Notably, an ^{40}Ar/^{39}Ar (sanidine) age for the same unit yielded an eruption age of 15.7 ± 0.2 Ma (2σ; Snow and Lux, 1999), an age that is strongly corroborated by age constraints in bounding units (e.g., Midttun,

2022; Miller et al., 2022). Compilations of data for quickly cooled volcanic and plutonic rocks indicate that a zircon U-Pb eruption age should be similar, within ~1% of the ^{40}Ar/^{39}Ar age (Schoene et al., 2006; Renne et al., 2010; Schmitz and Kuiper, 2013). However, the various MDA metrics show a spread of ~5.5 m.y. (Fig. 9D), ranging from 9.6 ± 0.1 Ma (2σ, YSG and MLA) to 15.0 ± 0.19 Ma (2σ, CAYP). The spread in MDAs also highlights an inherent problem with the MLA model: if the age difference between the youngest and second-youngest grains is significantly greater than their respective uncertainties, the MLA will default to the YSG age as a result (Figs. 9D–9F; Vermeesch, 2021). Although this result may be statistically sensible (Vermeesch, 2021), it may not be geologically reasonable. For example, young grains may have been introduced to a sample during collection or processing, resulting in anomalously young outliers. Alternatively, the presence of young grains in a sample may reflect Pb-loss that could have occurred either in source terranes or after deposition, either of which could produce precise but inaccurate young ages (Gehrels, 2014; Andersen et al., 2019). Some have suggested that Pb-loss is unlikely at the temperatures found in most sedimentary basins (e.g., Cherniak and Watson, 2001; Vermeesch, 2021), fueling an argument that many YSG ages should be considered permissible (e.g., Copeland, 2020), but others have demonstrated the pronounced effects of Pb-loss on lowering apparent zircon ages (e.g., Black, 1987; von Quadt et al., 2014; Watts et al., 2016; Herriott et al., 2019; Keller et al., 2019; Gehrels et al., 2020). Regarding data discussed herein, we dismiss the likelihood of Pb-loss in the source area of the tuffaceous material that sourced Cenozoic zircon grains because we interpret relatively rapid incorporation of ash-fall material into sedimentary systems. We also dismiss the likelihood of post-depositional Pb-loss because we do not observe uniform effects of Pb loss across all young grains in a sample, such as systematically high U concentrations associated with young grains (e.g., Gehrels et al., 2020).

In the case of sample ELM18DVTC-10, for which we expect a zircon U-Pb age close to an associated ^{40}Ar/^{39}Ar (sanidine) age of ca. 15.7 Ma, we consider the YSG and MLA of 9.60 ± 0.10 Ma (2σ) to be unreasonably young. In addition, we hesitate to arbitrarily omit young grain ages to modify the MLA calculation (e.g., Fig. 9D) for lack of analytical or geologic rationale that informs the number of young grains to omit, such as systematically high U concentrations in the youngest grains that might suggest effects of Pb-loss. Instead, we consider the CAYP to be a statistically reasonable and geologically appropriate, albeit more conservative, measure of MDA for the sample. The CAYP considers the entire distribution of Cenozoic zircon dates without the omission of grains on the tails of the distribution, and at the same time, it produces an age that is close to the associated ^{40}Ar/^{39}Ar (sanidine) age of the tuff (Fig. 9F).

Based on the above rationale, we systematically use either the MLA or CAYP metric as the most geologically *and* statistically appropriate measure of MDA. For most samples, the uncertainties of individual dates overlap at 2σ without strings of outliers that are obviously too young (Fig. 8), cases for which the MLA adequately considers the entire distribution of young ages. In samples characterized by multiple young outliers that skew the MLA toward one or two very young grains (e.g., Fig. 9D), the CAYP metric provides a
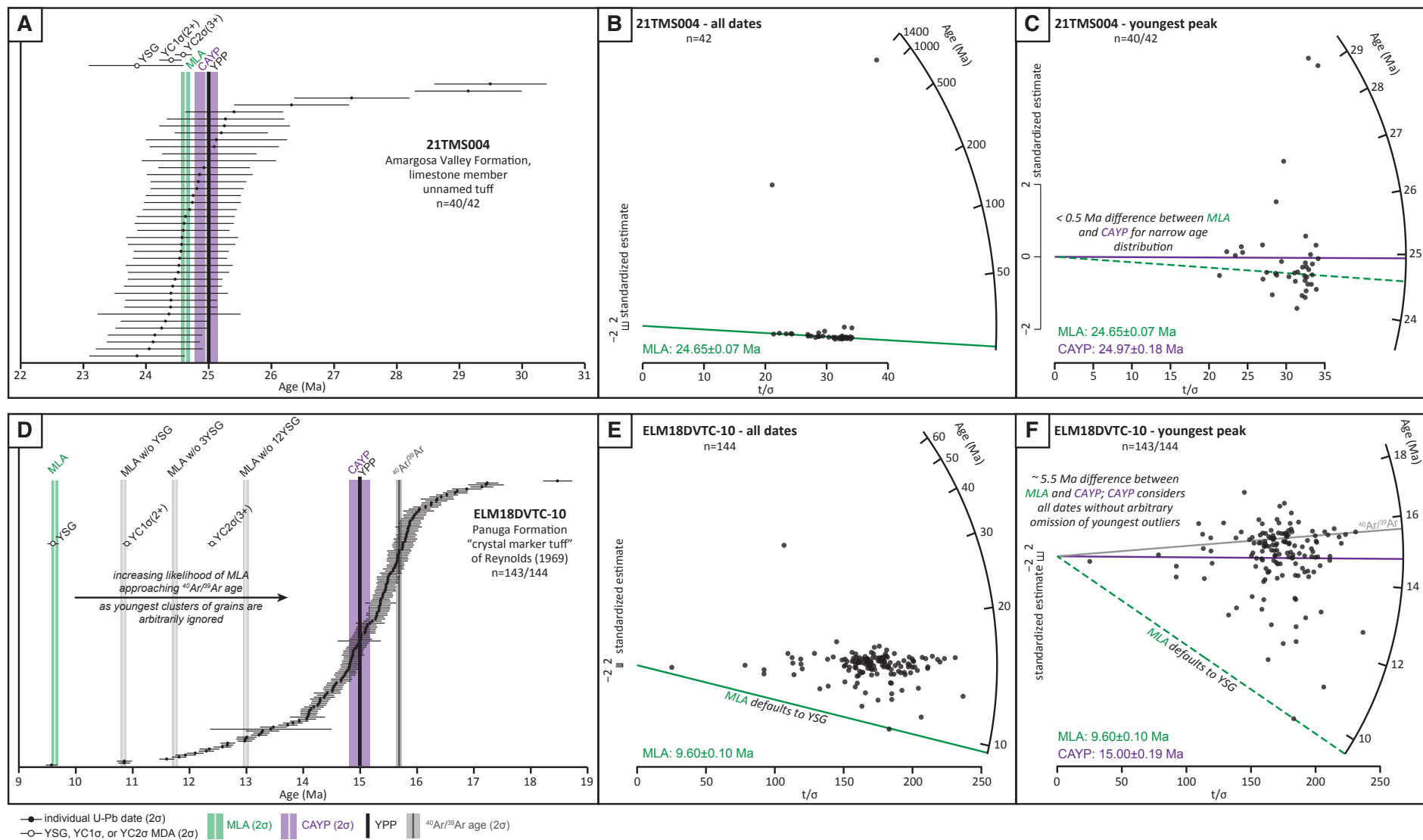
Figure 9. Graphical representation of the variability in maximum depositional age (MDA) metrics for two end-member examples of Cenozoic age distributions: (A–C) tuff sample 21TMS004 from the limestone member of the Amargosa Valley Formation (this study); (D–F) tuff sample ELM18DVTC-10 from the Panuga Formation (Miller et al., 2022). We consider sample 21TMS004 to be a "well-behaved" sample in which most MDA metrics converge to within 2σ uncertainty of one another due to the tight distribution of individual dates. While any MDA metric may be a reasonable choice, we prefer the maximum likelihood age (MLA). In contrast, sample ELM18DVTC-10 contains dates that form a normal distribution with skewed tails, resulting in MDAs that span >5 m.y. In this scenario, we consider the central age of the youngest peak (CAYP) as the most geologically appropriate MDA metric because it honors all ages in the distribution without the need for arbitrary omission of young ages in the tails of the distribution. ^{40}Ar/^{39}Ar age of Crystal Marker tuff from Snow and Lux (1999). YSG—youngest single grain; YPP—youngest graphical peak.

more conservative age that still considers the entire young distribution. We emphasize, however, that no one MDA metric is guaranteed to be appropriate for the interpretation of every detrital zircon age distribution. Depending on provenance or the number of analyses performed for a sample, some samples may not be characterized by large numbers of young dates, and metrics such as the YSG may yield a more appropriate MDA (e.g., sample EM-1 from the Eagle Mountain Formation of Niemi et al., 2001; Table 2; Niemi, 2013). Fundamentally, balance should be maintained between consistently employing MDA metrics that are both statistically rigorous and geologically reasonable, while also retaining flexibility to select alternatives for individual samples that may be characterized by limited young ages.

Sedimentation and Regional Volcanism

The presence of tuffs throughout the strata exposed on Bat Mountain and the abundance of Cenozoic zircon grains present in sandstones reveal a strong temporal relationship between regional volcanism and local sedimentation. Ultimately, this relationship is what permits development of a detailed chronology for the strata at Bat Mountain and correlation of those strata to others across the region (Fig. 10).

Figure 10 includes a graph of the ages of volcanic rocks exposed across the Great Basin as a function of latitude. It is well-established that volcanism generally expanded southward across the Great Basin during the Cenozoic (Armstrong and Ward, 1991; Christiansen and Yeats, 1992; Henry and John, 2013), with Eocene volcanism focused north of ~40°N, Oligocene volcanism north of ~38°N, and Miocene volcanism north of ~36°N (Fig. 10). Local volcanism associated with the southwestern Nevada and central Death Valley volcanic fields did not initiate until the middle Miocene, ca. 13 Ma (Fig. 10; Wright et al., 1991; Sawyer et al., 1994; Fridrich and Thompson, 2011). Given these relationships, the tuffs present throughout the stratigraphic succession at Bat Mountain are likely extrabasinal, emanating from late Oligocene to early Miocene caldera eruptions that were likely centered northeast of the study area. The extrabasinal origin of tuffs is further supported by their overall fine-grained nature and lack of welding or flow structures, which suggests deposition by ash-fall into mostly quiescent lacustrine environments. Not until deposition of the upper sandstone member of the Bat Mountain Formation (i.e., sample 21TMS013) did local volcanic centers, such as the central Death Valley volcanic field, become possible sources of tuffaceous material (Fig. 10).

Detrital zircon age distributions from sandstones also reflect volcanic activity that was nearly contemporaneous with deposition (e.g., Rossignol et al., 2019). Although each sample contains abundant Mesozoic and older ages, each also contains a relatively tight, unimodal and near-normal distribution of Cenozoic dates (Figs. 7 and 8). The MDAs interpreted for each sample are younger up-section and compatible with the ages of interstratified ash-fall tuffs (Figs. 3 and 11). These relationships suggest direct derivation of volcanogenic zircon during ash-fall events and/or remobilization of recently deposited ash-fall tuffs by high-energy sedimentary environments (Schwartz et al., 2021). Except for sample 21TMS011, the lack of more broadly distributed or multi-modal Cenozoic peaks supports this concept, indicating minimal sedimentary mixing of multiple volcanogenic deposits of differing ages prior to sandstone deposition.

Revised Chronology of the Amargosa Valley and Bat Mountain Formations

The new zircon U-Pb geochronology data for tuff and sandstone samples presented herein provide a revised and more detailed chronostratigraphic framework for the Amargosa Valley and Bat Mountain formations and their constituent members. The new ages supplement existing K/Ar and ^{40}Ar/^{39}Ar ages of tuffs by (1) establishing the age of the basal conglomerate member of each formation, (2) revising or confirming the ages of other lithostratigraphic members in each formation, and (3) organizing those ages in a coherent stratigraphic framework (Figs. 3 and 11).

Zircon U-Pb ages establish a middle Oligocene to early Miocene (ca. 28.5–18.5 Ma) age for the Amargosa Valley Formation (Fig. 10): the conglomerate and limestone members of the Amargosa Valley Formation were deposited primarily during the middle and late Oligocene, whereas deposition of the red sandstone member initiated near the Oligocene–Miocene boundary (ca. 22.5 Ma) and continued until ca. 18.5 Ma. New ages from this study are consistent with an existing K/Ar (biotite) age of a tuff (24.7 ± 0.3 Ma, 2σ; Çemen et al., 1985) near the base of the limestone member, ^{40}Ar/^{39}Ar (sanidine) ages of tuffs reported for the transition zone between the limestone and red sandstone members (22.57 ± 0.1 Ma, 2σ; Fridrich et al., 2012) and the top of the red sandstone member (21.58 ± 0.16 Ma, 2σ; Fridrich et al., 2012), and another K/Ar (biotite) age of a tuff (19.8 ± 0.2 Ma, 2σ; Çemen et al., 1985) near the top of the red sandstone member (Table 2). Altogether, the MDAs from this study indicate relatively rapid, undecompacted sedimentation rates for the conglomerate member (~115 m/m.y.) and red sandstone member (~105 m/m.y.) of the Amargosa Valley Formation, but a slower rate for the limestone member (~65 m/m.y.; Fig. 11). The rates for the two siliciclastic members are higher than, but on the same order as, the average rate of ~100 m/m.y. interpreted for the entire Amargosa Valley Formation (referred to as the Ubehebe Formation by Snow and Lux, 1999). Notably, the rates are an order of magnitude higher than those calculated for Eocene to early Oligocene intervals of the Titus Canyon Formation (~25 m/m.y.; Midttun, 2022), which suggests a late Oligocene increase in local subsidence and accommodation potentially related to an early phase of extension (Snow and Lux, 1999) in the Death Valley region.

Zircon U-Pb ages support a middle Miocene age (ca. 15.5–13.5 Ma) for the exposed parts of the Bat Mountain Formation (Fig. 10), consistent with regional correlations proposed by Snow and Lux (1999). Thus, the Kelley's Well Limestone that lies between the Amargosa Valley and Bat Mountain formations is constrained as early to middle Miocene in age and was deposited
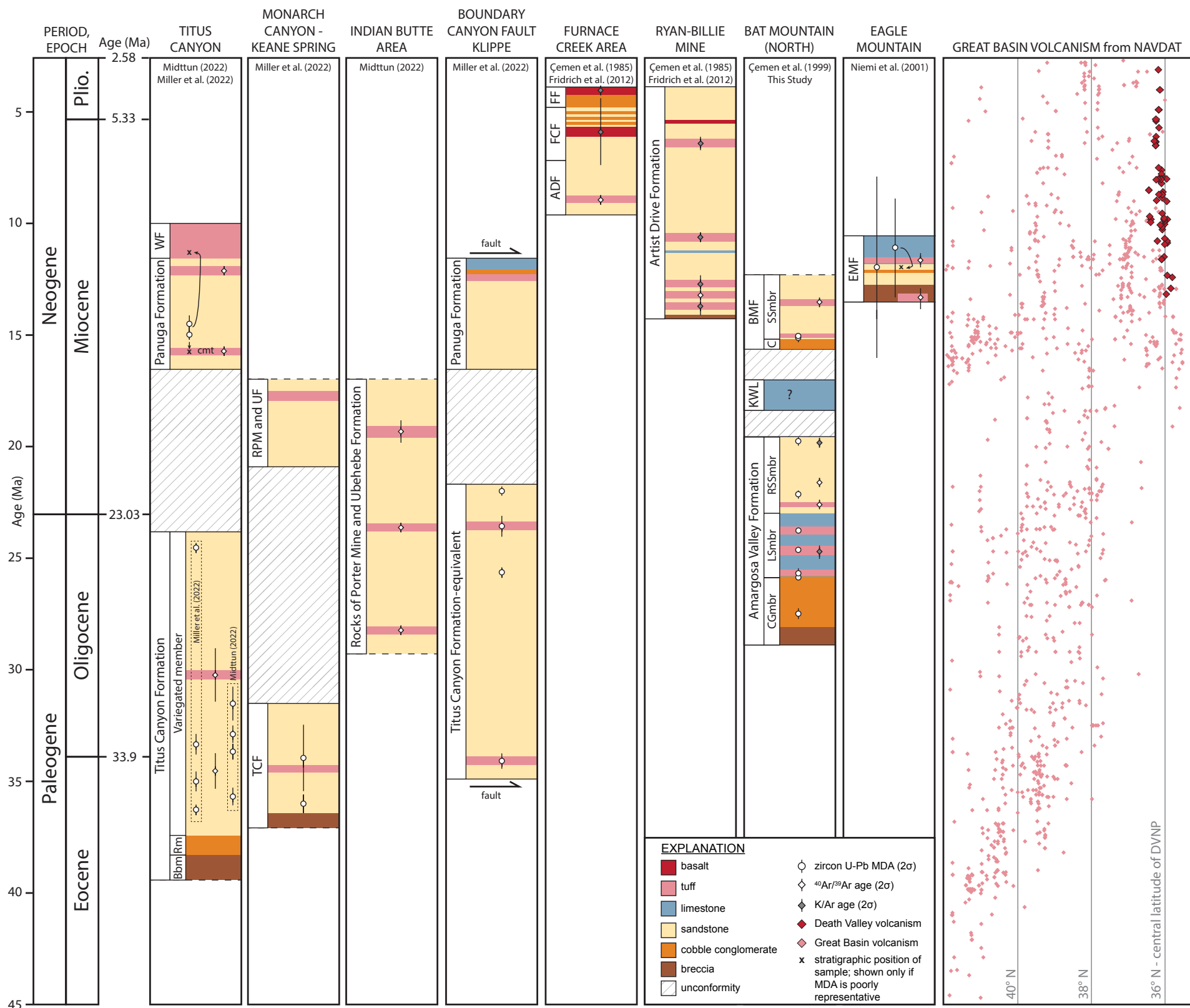
Figure 10. Correlation chart of Cenozoic stratigraphic successions found in the Grapevine-Funeral Mountains (e.g., Fig. 1) based on available K/Ar, ⁴⁰Ar/³⁹Ar, and U-Pb age constraints for those sections (Table 2). Stratigraphic data are also compared to K/Ar, ⁴⁰Ar/³⁹Ar, U-Pb, and fission track ages for Cenozoic igneous rocks of the Nevada sector of the Great Basin between 35°N and 42°N (compiled from NAVDAT, www.navdat.org) and the central Death Valley volcanic field (Wright et al., 1991). Geologic time scale of Walker et al. (2018). Stratigraphic abbreviations: ADF—Artist Drive Formation; Bbm—basal breccia member of the Titus Canyon Formation (Midttun, 2022); BMF—Bat Mountain Formation; C—conglomerate member of the Bat Mountain Formation; CGmbr—conglomerate member of the Amargosa Valley Formation; cmt—crystal marker tuff of Reynolds (1969); DVNP—Death Valley National Park; EMF—Eagle Mountain Formation (Niemi et al., 2001); FCF—Furnace Creek Formation; FF—Funeral Formation; KWL—Kelley's Well Limestone; LSmbr—limestone member of the Amargosa Valley Formation; Rm—redbed member of the Titus Canyon Formation (Midttun, 2022); RPM—Rocks of Porter Mine (Midttun, 2022); RSSmbr—red sandstone member of the Amargosa Valley Formation; SSmbr—sandstone member of the Bat Mountain Formation; TCF—Titus Canyon Formation; UF—Ubehebe Formation (Snow and Lux, 1999); WF—Wahguyhe Formation (Niemi, 2013). MDA—maximum depositional age.
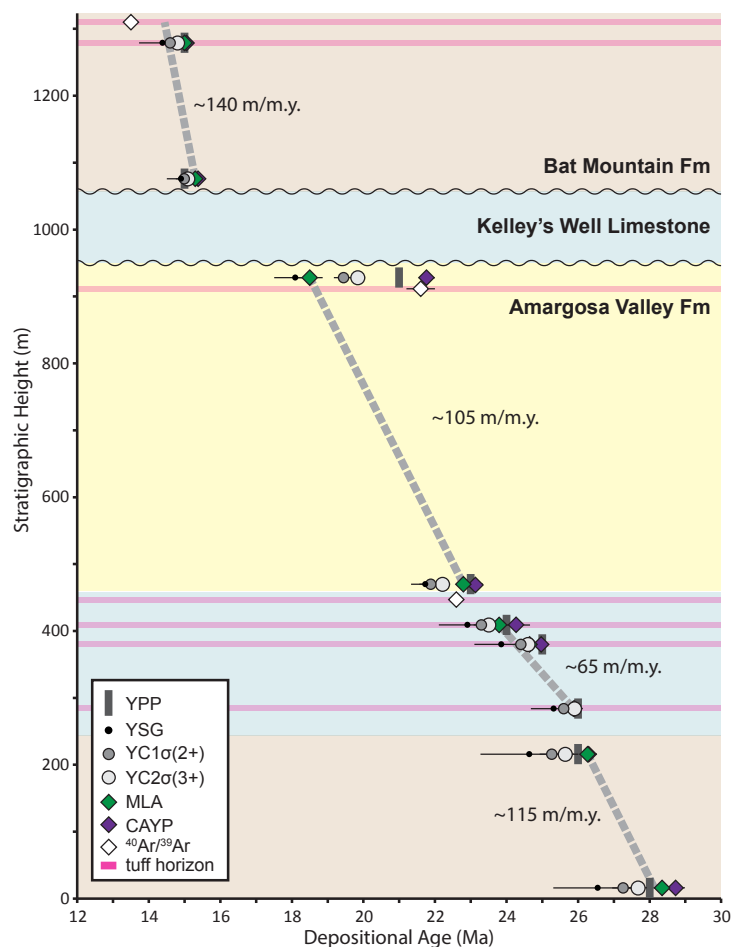
Figure 11. Age-depth plot for the Amargosa Valley and Bat Mountain formations shows the spread of possible maximum depositional ages (MDAs) for each sampled horizon of the formations. Approximate undecompacted sedimentation rates are shown by gray dashed lines, with rates calculated using the maximum likelihood age (MLA) at each horizon. CAYP—central age of the youngest peak; YSG—youngest single grain; YPP—youngest graphical peak.

sometime between ca. 18.5 Ma and 15.5 Ma (Fig. 10). Deposition of the conglomerate member of the Bat Mountain Formation initiated by ca. 15.5 Ma and was followed shortly by deposition of the sandstone member. These ages are compatible with an $^{40}Ar/^{39}Ar$ (sanidine) age of a tuff located higher in the sandstone member (13.52 ± 0.07 Ma, 2σ; Fridrich et al., 2012). The MDAs indicate undecompacted sedimentation rates of ~140 m/m.y., similar

to those calculated for the siliciclastic members of the Amargosa Valley Formation (Fig. 11). Although our calculated sedimentation rate is lower than the ~450 m/m.y. rate proposed by Snow and Lux (1999), it is likely that deposition of the Bat Mountain Formation was associated with increased subsidence and accommodation at this time due to regional extension (Snow and Lux, 1999).

Correlation to Other Cenozoic Strata of the Death Valley Region

Our new zircon U-Pb data and improved geochronology allow for enhanced correlations among Cenozoic strata exposed at Bat Mountain and other Cenozoic successions in the vicinity of eastern Death Valley National Park. Table 2 and Figure 10 summarize the age constraints for Cenozoic strata exposed along the northwest–southeast trend of the Grapevine and Funeral Mountains for sections located in the Titus Canyon, Monarch Canyon–Keane Spring, Indian Butte, Furnace Creek, Ryan-Billie Mine, Bat Mountain, and Eagle Mountain areas (Fig. 1). We reiterate that all MDAs from published zircon U-Pb data (Table 2) were recalculated according to the methods outlined herein to ensure consistent interpretation and comparison of MDAs. Similar to new samples that characterize Bat Mountain strata, we use the MLA or CAYP metric as a preferred MDA for samples from other successions.

Based on new ages for the conglomerate member of the Amargosa Valley Formation, the lower part of the Amargosa Valley Formation may be age-equivalent to upper parts of the Titus Canyon Formation where exposed in Titus Canyon (Fig. 10), as suggested by Fridrich et al. (2012). However, detrital zircon MDAs presented in two different studies of the Titus Canyon Formation yielded inconsistent upper age bounds for the unit: Midttun (2022) suggested an upper age of ca. 30.6 Ma (sample "Unit 38 Tuff"; reinterpreted herein as 32.89 ± 0.39 Ma based on the CAYP; Table 2), whereas Miller et al. (2022) suggested a much younger age of ca. 23.7 Ma (sample ELM18DVTC-7; reinterpreted herein as 24.53 ± 0.06 Ma based on the CAYP; Table 2). The discrepancy in the upper age of the Titus Canyon Formation at Titus Canyon remains unresolved. If the upper part of the Titus Canyon Formation in Titus Canyon is early–middle Oligocene (Midttun, 2022), the lower Amargosa Valley Formation is not correlative; if the upper part of the same section is late Oligocene (Miller et al., 2022), the lower Amargosa Valley Formation is correlative. Notably, the lower Amargosa Valley Formation is correlative to undifferentiated equivalents of the Titus Canyon Formation (after Miller et al., 2022) exposed in a klippe of the Boundary Canyon fault (Fig. 10).

The Amargosa Valley Formation is demonstrably correlative to lower parts of the informally named Rocks of Porter Mine (Midttun, 2022) and the Ubehebe Formation (Snow and Lux, 1999) where exposed in the Indian Butte area (Fig. 10). The Amargosa Valley Formation is also partly correlative to numerous, mostly unnamed Cenozoic sedimentary successions that were deposited throughout southern Nevada and southwestern Utah prior to locally erupted volcanic rocks in each region (e.g., Tschanz and Pampeyan, 1970; Ekren et al., 1977; Stewart, 1980; Taylor, 1993; Niemi, 2002; Lund Snee et al., 2021).

The Bat Mountain Formation is correlative to the Panuga Formation where exposed in Titus Canyon and in a klippe of the Boundary Canyon fault (Fig. 10; Miller et al., 2022). Uppermost exposures of the Bat Mountain Formation are also correlative to the lower parts of the Artist Drive Formation where exposed at Ryan-Billie Mine (Çemen et al., 1985; Fridrich et al., 2012), and lower parts of the Eagle Mountain Formation at Eagle Mountain (Fig. 10; Niemi et al., 2001).

These correlations support three general trends in regional Cenozoic sedimentation. (1) There is an apparent southward-younging of basin fills along the trend of the Grapevine-Funeral Mountains, in which the oldest Cenozoic strata that overlie Neoproterozoic–Paleozoic miogeoclinal strata become younger southward on average (Fig. 10). (2) A regional, early Miocene depositional hiatus is supported by a paucity of strata of that age along much of the Grapevine-Funeral Mountains trend, a local exception being the Kelley's Well Limestone at Bat Mountain and younger (but with ages relatively poorly constrained) parts of the Rocks of Porter Mine and the Ubehebe Formation exposed near Monarch Canyon and in the Indian Butte area (Fig. 10; after Midttun, 2022). (3) Regional deposition resumed by ca. 16 Ma along the length of the Grapevine-Funeral Mountains, supported by the preservation of thick stratal assemblages at Titus Canyon, the Furnace Creek area, Ryan-Billie Mine, Bat Mountain, and Eagle Mountain (Fig. 10). These regional trends are largely in support of tectonostratigraphic models that argue for two broad periods of Cenozoic deposition in the Death Valley area. The first, ca. 40–19 Ma, occurred prior to the onset of large-magnitude Basin and Range faulting (e.g., Çemen et al., 1999; Snow and Lux, 1999; Fridrich and Thompson, 2011; Miller et al., 2022) but may have been influenced by spatially limited normal faulting (e.g., Snow and Lux, 1999; Midttun, 2022). The second stage of Cenozoic deposition, beginning at ca. 15 Ma, was coeval with multi-stage Basin and Range faulting and core complex exhumation (Snow and Lux, 1999; Wright et al., 1999; Niemi et al., 2001; Miller and Pavlis, 2005; Fridrich and Thompson, 2011; Sizemore et al., 2019).

■ CONCLUSIONS

We present new zircon U-Pb geochronology data for a suite of sandstones and ash-fall tuffs that we used to develop a high-resolution chronostratigraphic framework for the Cenozoic strata exposed on Bat Mountain, located in the southern Funeral Mountains of California on the eastern border of Death Valley National Park (Figs. 1 and 2). Each sandstone sample yielded abundant Cenozoic zircon grains that we interpret to be volcanogenic and syn-depositional, derived from distant volcanic centers in the Great Basin during deposition of the Oligocene to early Miocene Amargosa Valley Formation and from local volcanic centers during deposition of the middle Miocene Bat Mountain Formation. A comparison of commonly used detrital zircon MDA metrics, benchmarked against K/Ar, ^{40}Ar/^{39}Ar, and zircon U-Pb ages of ash-fall tuffs, reveals that many MDA metrics—including the YSG, YC1σ(2+), YC2σ(3+), and YPP—provide unreasonably young or old values. Instead, the maximum likelihood estimation approach of Vermeesch (2021) consistently yields maximum likelihood ages

(MLAs) that are stratigraphically compatible with the ages of ash-fall tuffs. We introduce a variation on the MLA metric, the central age of the youngest peak (CAYP), that focuses exclusively on the youngest detrital zircon age peak in a distribution such that the calculation for the central age of the minimum age model is applied only to grain ages pertinent to determining depositional age (Fig. 5). We find that the MLA is best applied to age distributions without obvious outliers, whereas the CAYP provides a more conservative MDA for distributions with strongly skewed young tails or single dates that are anomalously young.

Detrital zircon MDAs and zircon U-Pb ages of ash-fall tuffs constrain deposition of the Oligocene–Miocene Amargosa Valley Formation to between ca. 28.5–18.5 Ma and the Miocene Bat Mountain Formation to between ca. 15.5–13.5 Ma (Figs. 3, 10, and 11). The age of the unconformity-bound Kelley's Well Limestone, stratigraphically positioned between the Amargosa Valley and Bat Mountain formations, remains loosely constrained to the early to middle Miocene and was deposited sometime between ca. 18.5 Ma and 15.5 Ma (Figs. 3, 10, and 11). These results suggest that the lower Amargosa Valley Formation may be age-equivalent to upper parts of the Eocene–Oligocene(?) Titus Canyon Formation and its equivalents in the southern Grapevine and northern Funeral Mountains (Fig. 10), but discrepancies regarding the upper age of the Titus Canyon Formation (Miller et al., 2022; Midttun, 2022) hinder their temporal relations. The Bat Mountain Formation is age-equivalent to strata exposed throughout the study area, including parts of the Panuga, Artist Drive, and Eagle Mountain formations (Fig. 10). While our results demonstrate the utility of detrital zircon MDAs in resolving the ages of Cenozoic strata in the Death Valley region, thereby permitting enhanced regional correlations, they also highlight the importance of geologic context in making statistically and geologically appropriate age interpretations.

REFERENCES CITED

Andersen, T., Elbug, M.A., and Magwaza, B.N., 2019, Sources of bias in detrital zircon geochronology: Discordance, concealed lead loss and common lead correction: Earth-Science Reviews, v. 197, p. 1–15, https://doi.org/10.1016/j.earscirev.2019.102899.

Armstrong, R.L., and Ward, P., 1991, Evolving geographic patterns of Cenozoic magmatism in the North American Cordillera: The temporal and spatial association of magmatism and metamorphic core complexes: Journal of Geophysical Research: Solid Earth, v. 96, no. B8, p. 13,201–13,224, https://doi.org/10.1029/91JB00412.

Bauer, A.M., Vervoort, J.D., and Fisher, C.M., 2020, Unraveling the complexity of zircons from the 4.0–2.9 Ga Acasta Gneiss Complex: Geochimica et Cosmochimica Acta, v. 283, p. 85–102, https://doi.org/10.1016/j.gca.2020.05.023.

Black, L.P., 1987, Recent Pb loss in zircon: A natural or laboratory-induced phenomenon?: Chemical Geology, v. 65, p. 25–33, https://doi.org/10.1016/0168-9622(87)90059-5.

Black, L.P., Kamo, S.L., Allen, C.M., Davis, D.W., Aleinikoff, J.N., Valley, J.W., Mundil, R., Campbell, I.H., Korsch, R.J., Williams, I.S., and Foudoulis, C., 2004, Improved $^{206}Pb/^{238}U$ microprobe geochronology by the monitoring of a trace-element-related matrix effect; SHRIMP, ID–TIMS, ELA–ICP–MS and oxygen isotope documentation for a series of zircon standards: Chemical Geology, v. 205, p. 115–140, https://doi.org/10.1016/j.chemgeo.2004.01.003.

Çemen, I., Wright, L.A., Drake, R.E., and Johnson, F.C., 1985, Cenozoic sedimentation and sequence of deformational events at the southeastern end of the Furnace Creek strike-slip fault zone, Death Valley region, California, *in* Biddle, K.T., and Christie-Blick, N., eds., Strike-Slip Deformation, Basin Formation, and Sedimentation: SEPM (Society for Sedimentary Geology) Special Publication 37, p. 127–141, https://doi.org/10.2110/pec.85.37.0105.

Çemen, I., Wright, L.A., and Prave, A.R., 1999, Stratigraphy and tectonic implications of the latest Oligocene and early Miocene sedimentary succession, southernmost Funeral Mountains, Death Valley region, California, *in* Wright, L.A., and Troxel, B.W., eds., Cenozoic Basins of the Death Valley Region: Geological Society of America Special Paper 333, p. 65–86, https://doi.org/10.1130/0-8137-2333-7.65.

Cherniak, D., and Watson, E., 2001, Pb diffusion in zircon: Chemical Geology, v. 172, no. 1–2, p. 5–24, https://doi.org/10.1016/S0009-2541(00)00233-3.

Christiansen, R.L., and Yeats, R.S., 1992, Post-Laramide geology of the U.S. Cordilleran region, *in* Burchfiel, B.C., Lipman, P.W., and Zoback, M.L., eds., The Cordilleran Orogen: Conterminous U.S.: Boulder, Colorado, Geological Society of America, The Geology of North America, v. G-3, p. 261–406, https://doi.org/10.1130/DNAG-GNA-G3.261.

Copeland, P., 2020, On the use of geochronology of detrital grains in determining the time of deposition of clastic sedimentary strata: Basin Research, v. 32, no. 6, p. 1532–1546, https://doi.org/10.1111/bre.12441.

Coutts, D.S., Matthews, W.A., and Hubbard, S.M., 2019, Assessment of widely used methods to derive depositional ages from detrital zircon populations: Geoscience Frontiers, v. 10, p. 1421–1435, https://doi.org/10.1016/j.gsf.2018.11.002.

Dickinson, W.R., and Gehrels, G.E., 2009, Use of U–Pb ages of detrital zircons to infer maximum depositional ages of strata: A test against a Colorado Plateau Mesozoic database: Earth and Planetary Science Letters, v. 288, p. 115–125, https://doi.org/10.1016/j.epsl.2009.09.013.

Ekren, E.B., Orkild, P.P., Sargent, K.A., and Dixon, G.L., 1977, Geologic map of Tertiary rocks, Lincoln County, Nevada: U.S. Geological Survey Miscellaneous Investigation Series Map I-1041, scale 1:250,000, https://doi.org/10.3133/i1041.

Fridrich, C.J., and Thompson, R.A., 2011, Cenozoic tectonic reorganizations of the Death Valley region, southeast California and southwest Nevada: U.S. Geological Survey Professional Paper 1783, 36 p., https://doi.org/10.3133/pp1783.

Fridrich, C.J., Thompson, R.A., Slate, J.L., Berry, M.E., and Machette, M.N., 2012, Geologic map of the southern Funeral Mountains including nearby groundwater discharge sites in Death Valley National Park, California and Nevada (1:50,000): U.S. Geological Survey Scientific Investigations Map SIM-3151, https://doi.org/10.3133/sim3151.

Galbraith, R.F., and Laslett, G., 1993, Statistical models for mixed fission track ages: Nuclear Tracks and Radiation Measurements, v. 21, no. 4, p. 459–470, https://doi.org/10.1016/1359-0189(93)90185-C.

Gehrels, G., 2014, Detrital zircon U-Pb geochronology applied to tectonics: Annual Review of Earth and Planetary Sciences, v. 42, p. 127–149, https://doi.org/10.1146/annurev-earth-050212-124012.

Gehrels, G., and Pecha, M., 2014, Detrital zircon U-Pb geochronology and Hf isotope geochemistry of Paleozoic and Triassic passive margin strata of western North America: Geosphere, v. 10, no. 1, p. 49–65, https://doi.org/10.1130/GES00889.1.

Gehrels, G., Giesler, D., Olsen, P., Kent, D., Marsh, A., Parker, W., Rasmussen, C., Mundil, R., Irmis, R., Geissman, J., and Lepre, C., 2020, LA-ICPMS U-Pb geochronology of detrital zircon grains from the Coconino, Moenkopi, and Chinle formations in the Petrified Forest National Park (Arizona): Geochronology, v. 2, p. 257–282, https://doi.org/10.5194/gchron-2-257-2020.

Gehrels, G.E., Valencia, V., and Ruiz, J., 2008, Enhanced precision, accuracy, efficiency, and spatial resolution of U-Pb ages by laser ablation-inductively coupled plasma-mass spectrometry: Geochemistry, Geophysics, Geosystems, v. 9, https://doi.org/10.1029/2007GC001805.

Gutenkunst, M., 2006, Stratigraphic and geochronologic analysis of Eocene–Miocene synextensional strata in the Grapevine and Funeral Mountains of southwestern Nevada and southeastern California: Implications for regional correlation of "pre-basin and range" stratigraphy [MS thesis]: West Lafayette, Indiana, Purdue University, 265 p.

Henry, C.D., and John, D.A., 2013, Magmatism, ash-flow tuffs, and calderas of the ignimbrite flareup in the western Nevada volcanic field, Great Basin, USA: Geosphere, v. 9, no. 4, p. 951–1008, https://doi.org/10.1130/GES00867.1.

Herriott, T.M., Crowley, J.L., Schmitz, M.D., Wartes, M.A., and Gillis, R.J., 2019, Exploring the law of detrital zircon: LA-ICP-MS and CA-TIMS geochronology of Jurassic forearc strata, Cook Inlet, Alaska, USA: Geology, v. 47, no. 11, p. 1044–1048, https://doi.org/10.1130/G46312.1.

Horstwood, M.S.A., Košler, J., Gehrels, G., Jackson, S.E., McLean, N.M., Paton, C., Pearson, N.J., Sircombe, K., Sylvester, P., Vermeesch, P., Bowring, J.F., Condon, D.J., and Schoene, B., 2016, Community-derived standards for LA-ICP-MS U-(Th-) Pb geochronology–Uncertainty propagation, age interpretation and data reporting: Geostandards and Geoanalytical Research, v. 40, p. 311–332, https://doi.org/10.1111/j.1751-908X.2016.00379.x.

Johnstone, S.A., Schwartz, T.M., and Holm-Denoma, C.S., 2019, A stratigraphic approach to inferring depositional ages from detrital geochronology data: Frontiers of Earth Science, v. 7, https://doi.org/10.3389/feart.2019.00057.

Keller, C.B., Boehnke, P., Schoene, B., and Harrison, T.M., 2019, Stepwise chemical abrasion–isotope dilution–thermal ionization mass spectrometry with trace element analysis of microfractured Hadean zircon: Geochronology, v. 1, p. 85–97, https://doi.org/10.5194/gchron-1-85-2019.

Košler, J., Fonneland, H., Sylvester, P., Tubrett, M., and Pedersen, R.B., 2002, U–Pb dating of detrital zircons for sediment provenance studies—A comparison of laser ablation ICPMS and SIMS techniques: Chemical Geology, v. 182, p. 605–618, https://doi.org/10.1016/S0009-2541(01)00341-2.

Košler, J., Sláma, J., Belousova, E., Corfu, F., Gehrels, G.E., Gerdes, A., Horstwood, M.S.A., Sircombe, K.N., Sylvester, P.J., Tiepolo, M., Whitehouse, M.J., and Woodhead, J., 2013, U-Pb detrital zircon analysis—Results of an inter-laboratory comparison: Geostandards and Geoanalytical Research, v. 37, p. 243–259, https://doi.org/10.1111/j.1751-908X.2013.00245.x.

Lund Snee, J.-E., Schwartz, T.M., and Colgan, J.P., 2021, Record of Paleogene sedimentary basin and fluvial system development in southern Nevada, USA: Geological Society of America Abstracts with Programs, v. 53, no. 6, https://doi.org/10.1130/abs/2021AM-368375.

Midttun, N., 2022, Timing, rates, and styles of Cenozoic tectonism in the Basin and Range and Lesser Caucasus: Linking observations of intracontinental deformation to geodynamic processes [Ph.D. thesis]: Ann Arbor, Michigan, University of Michigan, 230 p.

Miller, E.L., Raftrey, M.E., and Lund Snee, J.-E., 2022, Downhill from Austin and Ely to Las Vegas: U-Pb detrital zircon suites from the Eocene–Oligocene Titus Canyon Formation and associated strata, Death Valley, California, *in* Craddock, J.P., Malone, D.H., Foreman, B.Z., and Konstantinou, A., eds., Tectonic Evolution of the Sevier-Laramide Hinterland, Thrust Belt, and Foreland, and Postorogenic Slab Rollback (180–20 Ma): Geological Society of America Special Paper 555, p. 359–378, https://doi.org/10.1130/2021.2555(14).

Miller, M.B., and Pavlis, T.L., 2005, The Black Mountains turtlebacks: Rosetta stones of Death Valley tectonics: Earth-Science Reviews, v. 73, p. 115–138, https://doi.org/10.1016/j.earscirev.2005.04.007.

Murray, D.A., 2002, Oligocene to Lower Miocene stratigraphy and extensional basin development, southwestern Nevada and southeastern California [M.S. thesis]: West Lafayette, Indiana, Purdue University, 179 p.

Niemi, N.A., 2002, Extensional tectonics in the Basin and Range Province and the geology of the Grapevine Mountains, Death Valley region, California and Nevada [Ph.D. thesis]: Pasadena, California, California Institute of Technology, 337 p.

Niemi, N.A., 2013, Detrital zircon age distributions as a discriminator of tectonic versus fluvial transport: An example from the Death Valley, USA, extended terrane: Geosphere, v. 9, no. 1, p. 126–137, https://doi.org/10.1130/GES00820.1.

Niemi, N.A., Wernicke, B.P., Brady, R.J., Saleeby, J.B., and Dunne, G.C., 2001, Distribution and provenance of the middle Miocene Eagle Mountain Formation, and implications for regional kinematic analysis of the Basin and Range province: Geological Society of America Bulletin, v. 113, no. 4, p. 419–442, https://doi.org/10.1130/0016-7606(2001)113<0419:DAPOTM>2.0.CO;2.

Paces, J.B., and Miller, J.D., 1993, Precise U-Pb ages of Duluth Complex and related mafic intrusions, northeastern Minnesota: Geochronological insights to physical, petrogenic, paleomagnetic, and tectonomagmatic processes associated with the 1.1 Ga Midcontinent Rift system: Journal of Geophysical Research: Solid Earth, v. 98, no. B8, https://doi.org/10.1029/93JB01159.

Renne, P.R., Mundil, R., Balco, G., Min, K., and Ludwig, K.R., 2010, Joint determination of ^{40}K decay constants and $^{40}Ar*/^{40}K$ for the Fish Canyon sanidine standard, and improved accuracy for

^{40}Ar/^{39}Ar geochronology: Geochimica et Cosmochimica Acta, v. 74, p. 5349–5367, https://doi .org/10.1016/j.gca.2010.06.017.

Reynolds, M.W., 1969, Stratigraphy and Structural Geology of the Titus and Titanothere Canyons Area, Death Valley, California [Ph.D. thesis]: Berkeley, California, University of California– Berkeley, 310 p.

Rossignol, C., Hallot, E., Bourquin, S., Poujol, M., Jolivet, M., Pellenard, P., Ducassou, C., Nalpas, T., Heilbronn, G., Yu, J., and Dabard, M.-P., 2019, Using volcaniclastic rocks to constrain sedimentation ages: To what extent are volcanism and sedimentation synchronous?: Sedimentary Geology, v. 381, p. 46–64, https://doi.org/10.1016/j.sedgeo.2018.12.010.

Sawyer, D.A., Fleck, R.J., Lanphere, M.A., Warren, R.G., Broxton, D.E., and Hudson, M.R., 1994, Episodic caldera volcanism in the Miocene southwestern Nevada volcanic field: Revised stratigraphic framework, ^{40}Ar/^{39}Ar geochronology, and implications for magmatism and extension: Geological Society of America Bulletin, v. 106, no. 10, p. 1304–1318, https://doi.org/10.1130 /0016-7606(1994)106<1304:ECVITM>2.3.CO;2.

Saylor, B.Z., and Hodges, K.V., 1994, ^{40}Ar/^{39}Ar age constraints on the depositional history of the Oligocene Titus Canyon Formation, Death Valley, California: Geological Society of America Abstracts with Programs, v. 26, no. 2, p. 88.

Schmitz, M.D., and Bowring, S.A., 2001, U-Pb zircon and titanite systematics of the Fish Canyon Tuff: An assessment of high-precision U-Pb geochronology and its application to young volcanic rocks: Geochimica et Cosmochimica Acta, v. 65, p. 2571–2587, https://doi.org/10.1016 /S0016-7037(01)00616-0.

Schmitz, M.D., and Kuiper, K.F., 2013, High-precision geochronology: Elements, v. 9, no. 1, p. 25–30, https://doi.org/10.2113/gselements.9.1.25.

Schoene, B., Crowley, J.L., Condon, D.J., Schmitz, M.D., and Bowring, S.A., 2006, Reassessing the uranium decay constants for geochronology using ID-TIMS U-Pb data: Geochimica et Cosmochimica Acta, v. 70, p. 426–445, https://doi.org/10.1016/j.gca.2005.09.007.

Schwartz, T.M., and Souders, A.K., 2022, Zircon U-Pb data for tuffs and sandstones of the Cenozoic Amargosa Valley and Bat Mountain Formations exposed on Bat Mountain, southern Funeral Mountains, California, USA: U.S. Geological Survey Data Release, https://doi.org /10.5066/P982KK4D.

Schwartz, T.M., Schwartz, R.K., and Weislogel, A.L., 2019, Orogenic recycling of detrital zircon characterizes age distributions of North American Cordilleran strata: Tectonics, v. 38, p. 4320–4334, https://doi.org/10.1029/2019TC005810.

Schwartz, T.M., Surpless, K.D., Colgan, J.P., Johnstone, S.A., and Holm-Denoma, C.S., 2021, Detrital zircon record of magmatism and sediment dispersal across the North American Cordilleran arc system (28–48°N): Earth-Science Reviews, v. 220, https://doi.org/10.1016/j.earscirev.2021 .103734.

Sharman, G.R., and Malkowski, M.A., 2020, Needles in a haystack: Detrital zircon U-Pb ages and the maximum depositional age of modern global sediment: Earth-Science Reviews, v. 203, https://doi.org/10.1016/j.earscirev.2020.103109.

Sharman, G.R., Sharman, J.P., and Sylvester, Z., 2018, detritalPy: A Python-based toolset for visualizing and analysing detrital geo-thermochronologic data: The Depositional Record: A Journal of Biological, Physical and Geochemical Sedimentary Processes, v. 4, p. 202–215, https://doi.org/10.1002/dep2.45.

Sizemore, T., Wielicki, M.M., Çemen, I., Stockli, D., Heizler, M., and Robinson, D., 2019, Structural evolution of central Death Valley, California, using new thermochronometry of the Badwater turtleback: Lithosphere, v. 11, no. 4, p. 436–447, https://doi.org/10.1130/L1044.1.

Sláma, J., Košler, J., Condon, D.J., Crowley, J.L., Gerdes, A., Hanchar, J.M., Horstwood, M.S.A., Morris, G.A., Nasdala, L., Norberg, N., Schaltegger, U., Schoene, B., Tubrett, M.N., and Whitehouse, M.J., 2008, Plešovice zircon—A new natural reference material for U–Pb and Hf isotopic microanalysis: Chemical Geology, v. 249, p. 1–35, https://doi.org/10.1016/j.chemgeo.2007.11.005.

Snow, J.K., and Lux, D.R., 1999, Tectono-sequence stratigraphy of Tertiary rocks in the Cottonwood Mountains and northern Death Valley area, California and Nevada, in Wright, L.A., and Troxel, B.W., eds., Cenozoic Basins of the Death Valley Region: Geological Society of America Special Paper 333, p. 17–64, https://doi.org/10.1130/0-8137-2333-7.17.

Stewart, J.H., 1980, Geology of Nevada: Nevada Bureau of Mines and Geology Special Publication 4, 136 p.

Taylor, W.J., 1993, Stratigraphic and lithologic analysis of the Claron Formation in southwestern Utah: Utah Geological Survey Miscellaneous Publication 93–1, 52 p.

Tschanz, C.M., and Pampeyan, E.H., 1970, Geology and mineral deposits of Lincoln County, Nevada: Nevada Bureau of Mines and Geology Bulletin, v. 73?, 187 p.

Vermeesch, P., 2018, IsoplotR: A free and open toolbox for geochronology: Geoscience Frontiers, v. 9, p. 1479–1493, https://doi.org/10.1016/j.gsf.2018.04.001.

Vermeesch, P., 2021, Maximum depositional age estimation revisited: Geoscience Frontiers, v. 12, p. 843–850, https://doi.org/10.1016/j.gsf.2020.08.008.

von Quadt, A., Gallhofer, D., Guillong, M., Peytcheva, I., Waelle, M., and Sakata, S., 2014, U-Pb dating of CA/non-CA treated zircons obtained by LA-ICP-MS and CA-TIMS techniques: Impact for their geological interpretation: Journal of Analytical Atomic Spectrometry, v. 29, no. 9, p. 1618–1629, https://doi.org/10.1039/C4JA00102H.

Walker, J.D., Geissman, J.W., Bowring, S.A., and Babcock, L.E., compilers, 2018, Geologic Time Scale v. 5.0: Geological Society of America, https://doi.org/10.1130/2018.CTS005R3C.

Watts, K.E., Coble, M.A., Vazquez, J.A., Henry, C.D., Colgan, J.P., and John, D.A., 2016, Chemical abrasion-SIMS (CA-SIMS) U-Pb dating of zircon from the late Eocene Caetano caldera, Nevada: Chemical Geology, v. 439, p. 139–151, https://doi.org/10.1016/j.chemgeo.2016.06.013.

Wiedenbeck, M., Hanchar, J.M., Peck, W.H., Sylvester, P., Valley, J., Whitehouse, M., Kronz, A., Morishita, Y., Nasdala, L., Fiebig, J., and Franchi, I., 2004, Further characterisation of the 91500 zircon crystal: Geostandards and Geoanalytical Research, v. 28, p. 9–39, https://doi.org/10.1111 /j.1751-908X.2004.tb01041.x.

Workman, J.B., Menges, C.M., Page, W.R., Taylor, E.M., Ekren, E.B., Rowley, P.D., Dixon, G.L., Thompson, R.A., and Wright, L.A., 2002, Geologic map of the Death Valley ground-water model area: Nevada and California: U.S. Geological Survey Miscellaneous Field Studies Map MF, v. 2381-A, https://doi.org/10.3133/mf2381A.

Wright, L.A., and Troxel, B.W., 1993, Geologic map of the central and northern Funeral Mountains and adjacent areas, Death Valley region, southern California: U.S. Geological Survey IMAP 2305, https://doi.org/10.3133/i2305.

Wright, L.A., Thompson, R.A., Troxel, B.W., Pavlis, T.L., DeWitt, E.H., Otton, J.K., Ellis, M.A., Miller, M.G., and Serpa, L.F., 1991, Cenozoic magmatic and tectonic evolution of the east-central Death Valley region, California, in Walawender, M.J., and Hanan, B.B., eds., Geologic Excursions in Southern California and Mexico: Geological Society of America 1991 Annual Meeting, Guidebook, p. 93–127.

Wright, L.A., Greene, R.C., Çemen, I., Johnson, F.C., and Prave, A.R., 1999, Tectonostratigraphic development of the Miocene–Pliocene Furnace Creek Basin and related features, Death Valley region, California, in Wright, L.A., and Troxel, B.W., eds., Cenozoic Basins of the Death Valley Region: Geological Society of America Special Paper 333, p. 87–114, https://doi.org/10.1130/0-8137-2333-7.87.